Article

Composite Aerosol Optical Depth Mapping over Northeast Asia from GEO-LEO Satellite Observations

Soi Ahn [1], Sung-Rae Chung [1,*], Hyun-Jong Oh [1] and Chu-Yong Chung [2]

[1] National Meteorological Satellite Center (NMSC), Korea Meteorological Administration (KMA), Jincheon-gun 27803, Korea; jjahn@korea.kr (S.A.); hyunjong.oh@korea.kr (H.-J.O.)
[2] National Institute of Meteorological Sciences (NIMS), Korea Meteorological Administration (KMA), Seogwipo-si 63568, Korea; cychung@kma.go.kr
* Correspondence: csr@korea.kr; Tel.: +82-070-7850-5757

Abstract: This study aimed to generate a near real time composite of aerosol optical depth (AOD) to improve predictive model ability and provide current conditions of aerosol spatial distribution and transportation across Northeast Asia. AOD, a proxy for aerosol loading, is estimated remotely by various spaceborne imaging sensors capturing visible and infrared spectra. Nevertheless, differences in satellite-based retrieval algorithms, spatiotemporal resolution, sampling, radiometric calibration, and cloud-screening procedures create significant variability among AOD products. Satellite products, however, can be complementary in terms of their accuracy and spatiotemporal comprehensiveness. Thus, composite AOD products were derived for Northeast Asia based on data from four sensors: Advanced Himawari Imager (AHI), Geostationary Ocean Color Imager (GOCI), Moderate Infrared Spectroradiometer (MODIS), and Visible Infrared Imaging Radiometer Suite (VIIRS). Cumulative distribution functions were employed to estimate error statistics using measurements from the Aerosol Robotic Network (AERONET). In order to apply the AERONET point-specific error, coefficients of each satellite were calculated using inverse distance weighting. Finally, the root mean square error (RMSE) for each satellite AOD product was calculated based on the inverse composite weighting (ICW). Hourly AOD composites were generated (00:00–09:00 UTC, 2017) using the regression equation derived from the comparison of the composite AOD error statistics to AERONET measurements, and the results showed that the correlation coefficient and RMSE values of composite were close to those of the low earth orbit satellite products (MODIS and VIIRS). The methodology and the resulting dataset derived here are relevant for the demonstrated successful merging of multi-sensor retrievals to produce long-term satellite-based climate data records.

Keywords: composite aerosol optical depth (AOD); cumulative distribution function (CDF); Northeast Asia; AERONET; data fusion; retrieval algorithm

1. Introduction

Aerosols play an important role in the global energy budget, and atmospheric aerosol loading along with associated absorption and scattering properties is integral to the radiative forcing behind Earth's changing climate [1–4], while also modifying cloud properties and lifetimes [5,6]. This effect on the radiative energy balance is important for both estimating climate change and weather prediction [7,8]. Additionally, aerosols exhibit strong spatial and temporal variation and are generally concentrated in source regions [9,10]. In many developing countries, particulate matter (PM) accounts for the majority of air pollutants. In particular, fine PM with diameters that are generally 2.5 micrometers and smaller ($PM_{2.5}$) are associated with adverse human health impacts, and their high-concentration emissions from anthropogenic activities significantly increase haze events, deleteriously affecting both public health and traffic safety [11–14]. In Northeast Asia, the traffic associated with rapidly urbanizing and expanding cities is a major regional source of anthropogenic PM emissions [15]. Furthermore, aerosol events, characterized as having very high PM

concentrations from diverse sources, are increasing in frequency in the region [16–18]. Consequently, accurately assessing the progression of aerosols in Northeast-Asia is critical to monitoring of emissions locally and modeling to predict climate according to real-time satellite information, thus quickly avoiding direct and indirect damage and controlling human health and life.

Satellite-based remote sensing measurements allow systematic retrieval of optical aerosol properties at a local, regional, and global scales [1–20]. Aerosol optical depth (AOD) is defined as the integral of the amount of sunlight prevented from reaching the ground due to the absorbing and scattering of aerosols [21,22] and correlates strongly with aerosol amount [23]. AOD is a key parameter for various aerosol-related studies, such as radiative forcing and atmospheric correction of remote sensing imagery [24]. AOD estimates collected via satellite observation have the advantages of large spatial coverage and reliable, continuous measurements compared to ground-based data; therefore, the use of satellite-based imagery is an encouraging approach to monitor the aerosol pathways and loadings [1,10,25–27]. The primarily regional emissions and distributions of aerosols can affect the weather, air quality, and other regional effects with global consequences such as volcanic ash, forest fires [13,28]. Consequently, it is imperative that aerosol monitoring be consistent, with high spatial resolution and accuracy sufficient for resolving regional trends [29]. However, AOD retrievals are overall overestimated, especially East Asia because of the uncertainty. In particular, retrieval of the AOD using the MODIS latest Collection 6.1 data is uncertain in East Asia due to low signal-to-noise ratio as a result of high surface reflectivity in the spectral bands used by the algorithm. It is related to varying surface and atmospheric aerosol conditions, which become larger with increases in surface reflectance, especially wintertime basins, snow cover, desert surfaces [30,31]. Furthermore, the differences in the vertical distribution of scattering and absorbing aerosols within the same column may also cause -15% (scattering > absorbing) to 15% errors (scattering < absorbing) [32].

For air quality assessments, calculating AOD based on satellite imagery is optimal to monitor rapid changes in aerosol distribution caused by weather systems or human activities [33]. However, the present AOD products from single satellite sensors are insufficient due to the limited spatial coverage, in addition to sporadic cloud presence preventing aerosol detection. Multi-sensor AOD products are therefore imperative for monitoring aerosol distribution. It is worth noting that discrepancies exist among AOD products derived from different satellite sensors [34] caused by inconsistencies in retrieval assumptions, sensor viewing angles, spectral channels, spatial and temporal resolutions, polarizations required for atmospheric data, cloud filtering, etc. [35]. Although no two satellite AOD products yield consistent values of aerosol properties [36], different AOD products can be complementary for accuracy and spatiotemporal completion. Geosynchronous equatorial orbit (GEO) satellites are advantageous for their ability to observe a specific area continuously with high temporal resolution. Alternatively, low Earth orbit (LEO) satellites have relatively poor temporal resolution but contain higher accuracy. Thus, merging AOD products derived from both GEO and LEO satellite sensors could yield more comprehensive results [37]. Therefore, the spatiotemporal differences between different AOD products should be minimized to ensure a more comprehensive representation of natural phenomenon [38]. However, retrieving high-resolution AOD at varying scales is still a challenging task due to the low signal-to-noise ratio in sensing, algorithmic synthesis constraints, downscaling issues, and data gaps resulting from adverse impacts such as cloud contamination [39,40].

Accordingly, this study conducts a cumulative distribution function (CDF) fitting method [41] to merge AOD measurements. This method has several advantages, including that it does not require identification of independent and background data [42]. Reference data, however, are necessary as they are collocated with the satellite products and used to adjust the observational data in a straightforward process that corrects nonlinear differences by rescaling the target data towards the reference data and then fitting the

observational CDF data accordingly [43]. The method of merging GEO and LEO satellite observations was initially developed to provide users with a comprehensive tool to monitor long-range aerosol transport with potential forecasting applications. In the near future, these products will also be used for data assimilation, such as improving aerosol-affected satellite radiance values into operational weather forecast models.

In the present study, we examine the effect of merging the Aerosol Robotic Network (AERONET)-based correction and fitting correction to improve AOD products and present a spatiotemporal data composite framework for merging multisensory data. The CDF fitting method was used to compile satellite product data, with AERONET measurements serving as the reference. Section 2 describes the satellite and reference data used, the CDF fitting, the inverse distance weighting (IDE), and inverse composite weighting (ICW) methods adopted in this study. The explanation of the composite AOD and mapping images obtained, their validation results, and limitations are described in Section 3, and Section 4 presents a brief conclusion.

2. Data and Methods

Table 1 provides a detailed summary of the different satellites, sensors, and datasets used in generating the near real time (NRT), hourly composite AOD from 00:00 UTC to 09:00 UTC.

Table 1. Summary of satellites and instruments used in producing the composite AOD product.

Satellite	Instrument/Orbit	Scientific Dataset Name	Resolution	Repeat Coverage
Himawari-8	AHI/GEO	Hourly aerosol product at 500 nm	00:00–09:00 UTC, 5 km	10 min
COMS	GOCI/GEO	GOCI Yonsei Aerosol V2 product at 500 nm	00:00–07:00 UTC, 0.5 km	1 h
Aqua·Terra	MODIS/LEO	Deep_Blue_Aerosol_ Optical_Depth_550_ Land_Best_Estimate	01:30/04:30 UTC, 10 km	$2\times \text{day}^{-1}$
Suomi-NPP	VIIRS/LEO	VIIRS_Aeros_EDR_GEO_ALL	04:30 UTC, 6 km	$1\times \text{day}^{-1}$

2.1. Satellite Data

2.1.1. Himawari-8/AHI

Himawari-8, a GEO meteorological satellite, was launched on 7 October 2014, and has been operational since 7 July 2015 [44–46]. It utilizes the Advanced Himawari Imager (AHI) instrument, equipped with 16 spectral bands at center wavelengths ranging from 470 to 1330 nm and with a spatial resolution of 0.5–2 km. Particularly, the three visible bands (blue, green, and red; 470, 510, and 640 nm, respectively) and one near-infrared band (NIR, 860 nm) are sensitive to aerosol scattering and absorption and thus enable the retrieval of aerosol optical properties, including AOD and the Angstrom exponent (AE), over wide areas of Asia and Oceania with unparalleled frequency [47]. Its recent products have the ability to minimize cloud contamination in the retrieval of AHI Level 2 (L2) Version 2.0 10-min aerosol products [48,49]. The AHI-based AOD products have been under development with the most recent release of the Earth Observation Research Center (EORC) of the Japan Aerospace Exploration Agency (JAXA) P-tree monitoring system (http://www.eorc.jaxa.jp/ptree/index.html accessed on 10 March 2021) on L2, Level 3 (L3), and Level 4 (L4) AOD products. Himawari-8/AHI performs full-disk observations at 10-min intervals, and the Himawari-8 L2 AOD product is derived from these full-disk observations conducted during the daytime. The AHI product has undergone continuous evaluations with clear uncertainty ranges: $[\Delta\tau = -0.66\tau + 0.02, -0.34\tau + 0.16]$ over land and $[\Delta\tau = -0.24\tau + 0.03, 0.10\tau + 0.11]$ over ocean [50]. In the present study, 10-min interval L2 products provided by JAXA during 2016 (training data) and 2017 (analysis, validation data) were used.

2.1.2. COMS/GOCI

The Geostationary Ocean Color Imager (GOCI) on the Communication, Ocean, and Meteorological Satellite (COMS) was launched in 2010 as the first ocean color imager in geostationary orbit. Its observation domain is East Asia, and it takes measurements eight times per day from 00:30 UTC to 07:30 UTC [51]. GOCI collects data across eight visible channels (412, 443, 490, 555, 600, 680, 745, and 865 nm) at a spatial resolution of 0.5 km. Recently, the GOCI Yonsei aerosol retrieval (YAER) algorithm Version 2 was developed to improve the accuracy of aerosol detection, surface reflectance, and wind speed using a climatological database from the multi-year GOCI dataset and reanalysis wind speed data [52]. The GOCI AOD product has an expected error of $\Delta \tau = \pm 0.137 \tau + 0.073$ overland and $\Delta \tau = \pm 0.185 \tau + 0.037$ over ocean [53]. The hourly GOCI data from 2016 (training data) and 2017 (analysis, validation data) were used for this study.

2.1.3. Terra, Aqua/MODIS

The Moderate Resolution Imaging Spectroradiometer (MODIS) is a LEO sensor with the ability to characterize the spatiotemporal global aerosol fields. Unlike previous satellite sensors discussed above in this paper with insufficient spectral diversity, MODIS has the ability to retrieve aerosol optical depth and aerosol size parameters with great accuracy [54]. MODIS data on the Aqua and Terra satellites have 36 spectral bands, with center wavelengths between 410–1450 nm [55]. MODIS-based AOD products have been under constant development, and the most recently released is the Collection 6 L2 AOD product [56–58]. In general, AOD values are retrieved by comparing the reflectance from the solar bands to a reference table of measured reflectance based on sun-satellite geometry, surface reflectance, and aerosol type [59]. The MODIS AOD product has a predicted uncertainty of $\Delta \tau = \pm 0.05 \pm 0.15 \tau$ (Dark Target, DT), $\Delta \tau = \pm 0.20 \pm 0.05 \tau$ (Deep Blue, DB) overland [55,59–61], $\Delta \tau = 0.03 \pm 0.05 \tau$ over ocean [59]. The L2 MOD04 and MYD04 data from 2016 (training data) and 2017 (analysis data) were used for this study [62].

2.1.4. Suomi-NPP/VIIRS

The heritage polar-orbital sensors, MODIS and Multi-angle Imaging Spectroradiometer (MISR), are nearing the end of their lifespans. To continue their legacy of global observation, the Suomi National Polar-orbiting Partnership (S-NPP) launched the Joint Polar Satellite System (JPSS), the first LEO satellite in the series of the United States next generation polar-orbiting operational environmental satellite system, on 28 October 2011 [63–66]. Daily global aerosol products, similar to those traditionally provided by MODIS at near-daily global coverage, are produced from observations of the visible infrared imaging radiometer suite (VIIRS), one of the instruments onboard. Due to its wider swath width, VIIRS does not have the orbital gaps near the equator that occur with MODIS, and it captures aerosol plumes more accurately along the edges of the scan that MODIS occasionally misses. The VIIRS aerosol products are derived primarily from the radiometric channels covering the visible spectrum through the shortwave infrared (SWIR) wavelengths (412–2250 nm). The product includes pixel-level AOD (~750 m) values and is considered an intermediate product (IP) to the AOD Environmental Data Record (EDR) at ~6 km resolution, as aggregated from the finer-resolution IP products. The VIIRS product has undergone continuous evaluations with uncertainty ranges: $[\Delta \tau = -0.470 \tau - 0.01 (lower\ bound),\ -0.0058 \tau + 0.09 (upper\ bound)]$ overland and $[\Delta \tau = -0.238 \tau + 0.01 (lower\ bound),\ 0.194 \tau + 0.048 (upper\ bound)]$ over ocean [63]. In this study, EDR data from 2016 (training data) and 2017 (analysis, validation data) were used.

2.1.5. AERONET

The network of ground-based AERONET sun–sky radiometers provide long-term observations of aerosol products, including spectral AOD [67,68], particle size distribution, and complex refractive indices for the atmospheric column across remote locations [69]. It uses Cimel sun/sky radiometers that take measurements of the direct sun and dif-

fused sky radiances across 340–1020 nm and 440–1020 nm spectral ranges, respectively [70]. AERONET provides columnar AODs over both land and ocean, but the values are restricted to point observations [71,72]. Despite the limited spatial coverage of ground-based aerosol remote sensing, its wide angular and spectral measurements of solar and sky radiation provide reliable and continuous data on aerosol optical properties [73]. Due to strong processing standards and low levels of uncertainty [24,74,75], AERONET AOD measurements have been considered as "ground truth" for calibrating and verifying satellite-based AOD retrieval products [61,76]. There are three levels of AERONET standard AOD products: Level 1.0, unscreened with possible cloud contamination; Level 1.5, cloud screened; and, Level 2.0, cloud screened and quality assured [18]. The AERONET provides a spectral AOD with low uncertainty (~0.01–0.02) under cloud-free conditions, by observing [67]. In this study, AERONET Level 2.0 AOD measurements from 27 sites located in East-Asia (Figure 1) were collected from January 2016 to July 2017 (http://aeronet.gsfc.nasa.gov/ accessed on 10 March 2021) to evaluate satellite-based AOD retrievals. AERONET site-specific details are listed in Table 2.
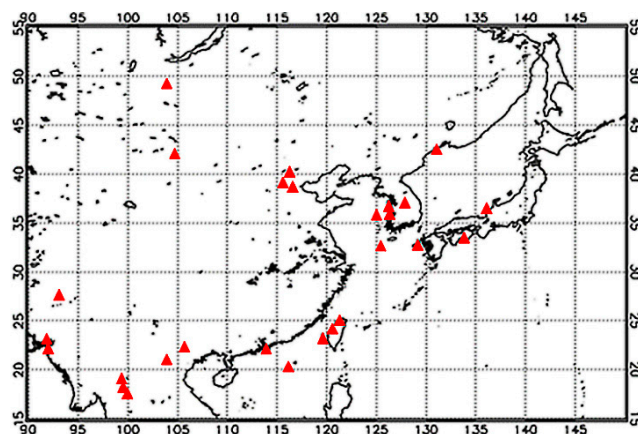

Figure 1. Locations of the 27 selected Aerosol Robotic Network (AERONET) sites used for comparisons of satellite AOD.

2.2. Methods

CDFs were used to estimate error statistics of satellite data compared to AERONET information across Northeast Asia. The range was extended across Northeast Asia by applying IDW using coefficients for each satellite, derived from the CDF. To increase accuracy, the root mean square error (RMSE) generated in each error range was composited using ICW.

2.2.1. Cumulative Distribution Function

CDFs were used to adjust GEO-LEO satellite AOD values according to AERONET ground measurements. This method is particularly useful for approximating and facilitating data analysis of information obtained from different sources [77]. In previous studies, CDFs have been used for fitting correction between satellite products and standardized data. The fitting technique enhances the performance of the output using a nonlinear, linear fitting method, threshold modification, and boundary value adjustment for the coefficients [34,77–81].

The application of CDFs for composite AOD data with satellite observation analysis is described by the flowchart in Figure 2. The observational and reference data for 2016 were selected to ensure sufficient information for applying the CDF [80]. CDF fitting was applied to each of the 27 AERONET site datasets for 2016, and an example of the results is shown in Figure 3, which displays CDF curves of AOD estimates from AHI, GOCI, MODIS, and VIIRS. It was expected that the curves from different products are more readily comparable than raw data values. The sequence of this method divided the

piece-wise polynomial CDF curve into several segments, performing polynomial regression analysis for each segment, and finally using the cubic equation to rescale the data falling into different segments (Equation (1)):

$$\text{AOD CDF Regression} = a_0 + a_1\, \text{AOD} + a_2\, \text{AOD2} + a_3\, \text{AOD3} \tag{1}$$

where the regression coefficients a_0, a_1, a_2, and a_3 are obtained through the fitting procedure, and new AOD values were calculated (Tables A1–A4).

Table 2. AERONET site details.

AERONET Sites	Longitude (Degree)	Latitude (Degree)	Elevation (m)
Anmyon	126.330	36.539	47
Baengnyeong	124.630	37.966	136
Beijing-CAMS	116.317	39.933	106
Beijing	116.381	39.754	36
Bhola	90.750	22.167	3
Chen-Kung_Univ.	120.217	23.000	50
Chiang_Mai_Met_Sta	98.972	18.771	312
Dalanzadgad	104.419	43.577	1470
Dhaka_Univ.	90.398	23.728	34
Dongsha-Island	116.729	20.699	5
Doi-Ang-Khang	99.045	19.932	1536
EPA-NCU	121.185	24.968	144
Fukuoka	130.475	33.524	30
Gangneung-WNU	128.867	37.771	60
Gosan_SNU	126.162	33.292	72
Hongkong_PolyU	114.117	22.483	40
Irkutsk	103.087	51.800	670
NGHIA_DO	105.800	21.048	40
Noto	137.137	37.334	200
Omkoi	98.432	17.798	1120
Seoul_SNU	126.951	37.458	116
Shirahama	135.357	33.693	10
Son_La	103.905	21.332	683
Taipei_CWB	121.500	25.030	26
Ussuriysk	132.163	43.700	280
XiangHe	116.962	39.754	36
Yonsei_Uni.	126.935	37.564	88

AOD values of the CDF curves were divided into 0.1 intervals from 0 to 4 to define 40 segments. The AOD values from AHI, GOCI, MODIS and VIIRS curves were plotted against the reference AERONET data, and then the scaling polynomial equations for each segment were obtained. Next, the segmented CDF curves of AHI, GOCI, MODIS and VIIRS were rescaled against the AERONET data for all satellite-derived data outside the range of the CDF curves. The results indicated that the rescaling process did not affect the variations of satellite-based products but rather imposed the value ranges of AERONET data.

2.2.2. Inverse Distance Weighting (IDW)

The IDW method is based on Tobler's First Law of Geography, where closer points are given larger weights [82,83]; thus, the influence of a known point declines with increasing distance. Weights are inversely proportional to the square of the distance [84–86], and the IDW was calculated according to Equation (2):

$$X(x_0) = \frac{\sum_{i=1}^{N} X(x_i)\omega_i}{\sum_{i=1}^{N} \omega_i} \tag{2}$$

where x_0 is the location of an estimated point, x_i ($i = 1, \dots , N$) are the locations of known points (i.e., satellite data), and the estimated value $X(x_0)$ is the weighted average of N measured values, $X(x_i)$. The weight or influence of each known data point was calculated as, $w_i = d_{0,i}{}^{-p}$, where w is weight, d is the Euclidian distance between the estimated and known points (i), and p is exponential power parameter. Lloyd [87] found that as the value of p increases, the estimation results become more similar to the value of the closest known point. Since the coefficient of the AERONET site produced using the CDF is a point coefficient, it does not represent the values of Northeast Asia. Therefore, the coefficients of Northeast Asia were reproduced using IDW with the CDF coefficients.
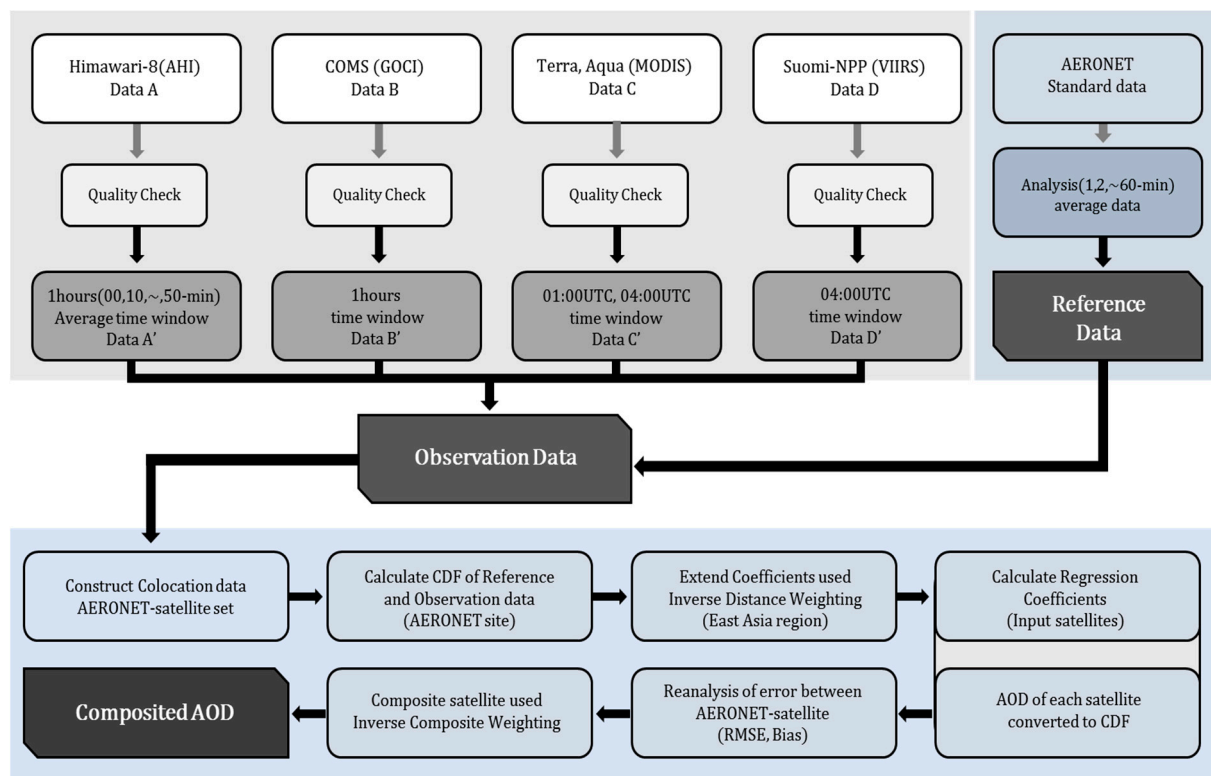

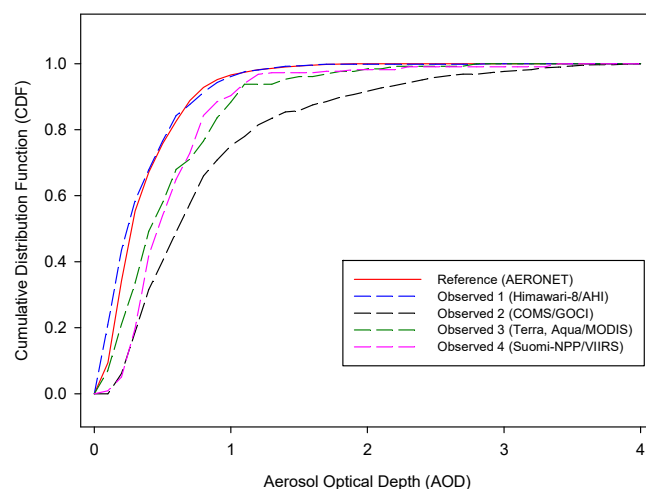**Figure 2.** Flow chart of composite AOD CDF algorithms.

Figure 3. Cumulative distribution functions (CDFs) of AOD derived from AERONET (reference data), corresponding to AODs derived remotely from satellite imagery for Anmyondo during 2016 (training data).

2.2.3. Inverse Composite Weighting (ICW)

Errors between satellite and reference AERONET data remained after applying CDFs. The delta value of each satellite refers to the RMSE value obtained through error analysis after applying the IDW method. It is performed the error correction to merge more accurate values. In order to reduce this issue, statistical errors were estimated by ICW according to Equation (3):

$$ICW = \frac{\left(\frac{1}{\Delta_1{}^2} AHI + \frac{1}{\Delta_2{}^2} MODIS + \frac{1}{\Delta_3{}^2} VIIRS + \frac{1}{\Delta_4{}^2} GOCI \right)}{\left(\frac{1}{\Delta_1{}^2} + \frac{1}{\Delta_2{}^2} + \frac{1}{\Delta_3{}^2} + \frac{1}{\Delta_4{}^2} \right)} \tag{3}$$

where $\Delta_1 = 0.80$, $\Delta_2 = 0.90$, $\Delta_3 = 0.91$, $\Delta_4 = 0.85$.

2.2.4. Composite AOD

In order to generate a NRT composite of AOD, we used the corrected GEO (AHI and GOCI) and LEO (MODIS, VIIRS) AOD products processed from 00:00 UTC to 09:00 UTC each day. LEO AODs were generated when they passed through Northeast Asia and merged with GOCI values obtained during daytime (GOCI data was acquired from 00:00 to 07:00 UTC at 1 h intervals for the region from 21.615°–46.971°N, 111.37°–148.548°E). AHI is the only data source available from 08:00 to 09:00 UTC, so the corresponding composites contained only the corrected AHI AOD (1 h interval, centered at 10.00°–60.00°N, 90.0°–150.0°E). AOD products from GEO and LEO sensors were rearranged and averaged across Northeast Asia. To that end, each satellite product was remapped on a unified grid since the sensors had different spatial resolutions and coordinate systems. Each satellite product was interpolated based on the 2 km spatial resolution of AHI. A nearest neighbor approach was used to interpolate all AOD retrievals on GEO product grids. These composite AOD maps were then merged and used to generate hourly final products.

2.2.5. HYSPLIT Trajectory

The Hybrid Single-Particle Lagrangian Integrated Trajectory (HYSPLIT) model is a computer model developed by the National Oceanic and Atmospheric Administration (NOAA) Air Resources Laboratory used to compute atmospheric transportation via air parcel trajectories and deposition or dispersion of atmospheric pollutants [88–98]. One of its most common applications is a back-trajectory analysis to determine the origin of air masses and locate source-receptor relationships, and it was used here to generate a probability map of the areas around a receptor site for selected aerosol episodic events. The meteorological input for the trajectory model was the GDAS (Global Data Assimilation) dataset (reprocessed from National Centres for Environmental Prediction (NCEP) by Air Resources Laboratory). These trajectories were computed at 1500 m altitudes for dust event in 2017.

3. Results and Discussion

3.1. CDF Fitting

For merging products of AHI, GOCI, MODIS, and VIIRS, CDFs were applied to the 27 AERONET sites for the entirety of 2016. The 2016 data were used for error analysis and the derivation of the regression equations, while the 2017 data were used for application and verification of the composite field for independent experimentation. CDFs were also applied to individual grid cells for increasing the accuracy of AOD. An example of the AOD CDF curve for the Anmyondo site (36.539°N, 126.33°W) is shown in Figure 3. The regression coefficients for each of the 27 points were calculated, and Figure 4 shows a piece-wise linear CDF fitting at Anmyondo across all satellite imagers analyzed for 2016. The satellite-based regression results revealed the same patterns as the observation data. GEO satellites are capable of constant observation at fixed locations on hourly or sub-hourly timescales [99], while LEO satellites have a return time of 1–2 times per day

for a specific area, translating into large differences in observation number. Thus, there is a lack of collocation data for LEO satellites. Nevertheless, the same polynomials were used to minimize the variability effect of aerosols and maintain the identity of the composite field in this study. The validation data for the AERONET sites were individually analyzed to compile the results for each site in 2016 (training data). The spatial distribution of the statistical evaluations is presented in Table 3, including pre- and post-CDF RMSE values (Figure 5). Overall, analysis results across all AERONET sites showed a post-CDF statistical error less than those of the original data. Error statistics of the satellite-based products were larger than those of the ground-based, and the CDF application decreased estimated AOD concentrations, effectively reducing error [100]. In terms of satellite products, LEO (MODIS and VIIRS) AOD estimates underwent insignificant changes with CDF application (Figure 5c,d, respectively), whereas GEO (AHI and GOCI) products benefitted greatly from the CDF, particularly over southern China (Figure 5a,b, respectively). However, the RMSE of collocated AHI data compared to AERONET AOD values was greatest across the Chinese sites, including Beijing and XiangHe. RMSE values of MODIS and VIIRS were higher than those of the Korean and Japanese AERONET sites. Due to the relatively narrow observation domain of GOCI, only 15 AERONET sites were collocated, and the error statistics show a good match with ground measurements for all locations, except the Chinese sites [101–105].
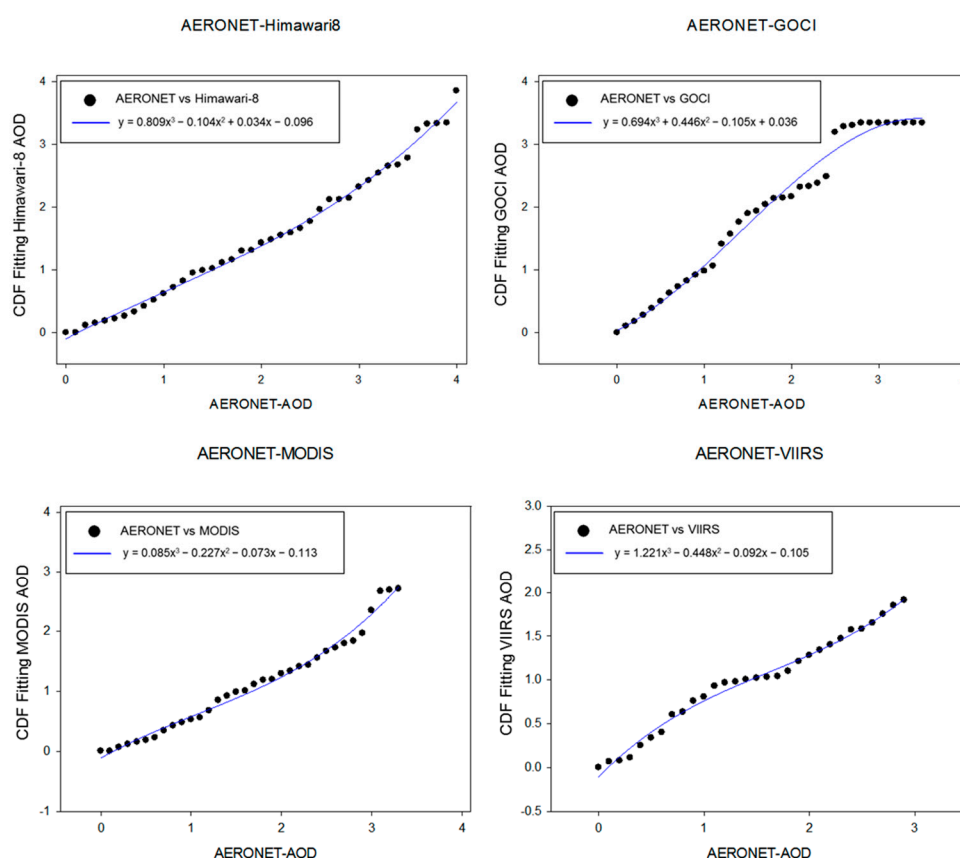

Figure 4. Plots of satellites AOD against Anmyondo AERONET site data during 2016 (training data): (**a**) Himawari-8/AHI, (**b**) COMS/GOCI, (**c**) Aqua Terra/MODIS, and (**d**) Suomi-NPP/VIIRS.

Table 3. Statistical error analysis (RMSE) for each satellite imager based on the selected AERONET sites, before/after applying the CDF method.

AERONET Sites	AHI	GOCI	MODIS	VIIRS
Anmyon	0.22/0.17	0.15/0.09	0.13/0.09	0.11/0.10
Baengnyeong	0.21/0.16	0.11/0.09	0.12/0.11	0.12/0.11
Beijing-CAMS	0.32/0.28	0.28/0.27	0.19/0.18	0.18/0.18
Beijing	0.32/0.28	0.28/0.27	0.19/0.18	0.18/0.18
Bhola	0.23/0.21	-	0.18/0.15	0.17/0.15
Chen-Kung_Uni.	0.16/0.09	0.21/0.09	0.09/0.08	0.09/0.08
Chiang_Mai_Met_Sta	0.24/0.18	-	0.16/0.14	0.14/0.13
Dalanzadgad	0.22/0.09	-	0.07/0.07	0.08/0.07
Dhaka_Uni.	0.32/0.28	-	0.13/0.11	0.13/0.12
Dongsha-island	0.14/0.12	-	0.08/0.08	0.07/0.07
Doi-Ang-Khang	0.16/0.15	-	0.19/0.15	0.17/0.14
EPA-NCU	0.28/0.18	0.22/0.08	0.09/0.09	0.09/0.09
Fukuoka	0.09/0.08	0.09/0.07	0.08/0.08	0.08/0.08
Gangneung-WNU	0.12/0.11	0.16/0.14	0.13/0.11	0.12/0.10
Gosan_SNU	0.13/0.11	0.17/0.14	0.06/0.05	0.08/0.06
Hongkong_PolyU	0.22/0.15	0.20/0.17	0.17/0.11	0.17/0.12
Irkutsk	0.19/0.09	-	0.04/0.04	0.04/0.04
NGHIA_DO	0.17/0.14	-	0.15/0.12	0.14/0.12
Noto	0.09/0.09	0.05/0.05	0.07/0.07	0.07/0.07
Omkoi	0.16/0.13	-	0.14/0.12	0.14/0.12
Seoul_SNU	0.22/0.16	0.18/0.09	0.11/0.08	0.07/0.07
Shirahama	0.08/0.08	0.06/0.06	0.09/0.08	0.07/0.06
Son_La	0.11/0.07	-	0.15/0.12	0.16/0.13
Taipei_CWB	0.11/0.10	0.21/0.18	0.18/0.15	0.17/0.16
Ussuriysk	0.11/0.09	0.09/0.08	0.09/0.09	0.08/0.08
XiangHe	0.34/0.30	0.29/0.28	0.26/0.24	0.26/0.24
Yonsei_Uni.	0.21/0.17	0.08/0.07	0.09/0.08	0.08/0.07

3.2. Performance of Composite AOD Products

3.2.1. Composite Temporal Variability and Satellite Retrieval Accuracy

The temporal variations of composite and satellite AOD accuracy were explored on a seasonal scale. The dominant aerosol types differ from spring (March, April, May; MAM), summer (June, July, August; JJA), fall (September, October, November; SON), and winter (December, January, February; DJF). In the spring, dust storms are a significant factor, and biomass burning in the summer contributes heavily to the aerosol load. Moreover, stable weather conditions in the winter can induce the accumulation of aerosols and allow severely polluted air to settle for several days at a time. Seasonal changes in surface reflectance can also affect the performance of aerosol retrievals [106]. Therefore, it was essential to account for the effect of seasonal variation on satellite and composite AOD estimates. (Figure A1). Quantitative metrics of accuracy, including the number of satellites and AERONET colocations (N), root mean square error (RMSE), mean bias (MB), mean absolute error (MAE), and the correlation coefficient (R) were used to assess satellite performance, and Table A5 summarizes these statistics across the seasons. VIIRS showed strong agreement with AERONET AOD values in the summer, with the highest R value observed, and an RMSE of 0.15. VIIRS also showed high correlations in the fall and spring, producing the highest overall accuracy values of all satellites. These VIIRS seasonal AOD accuracies were ranked as summer > fall > spring > winter, similar to the results found previously [107]. MODIS comparisons yielded a linear regression slope of 0.69 in the fall, and 0.68 in the winter and, along with the negligible intercept, put the relationship very close to the one-to-one line. The high R, low RMSE, and low MB demonstrated that MODIS AOD estimates are consistent with AERONET site measurements. Contrarily, AHI fall performance was worse than the other seasons. Additionally, AHI wintertime performance also yielded a low R value, and the same is true for winter GOCI AOD products. Al-

ternatively, AHI and GOCI performed better in summer than in the other three seasons. The analysis thus indicated that AHI and GOCI aerosol retrievals are significantly influenced by seasonal variations of surface reflectance and aerosol types [108], and the change of single scattering albedo led to large MB [109]. The composite AOD model developed in this study showed lower overall accuracies than MODIS and VIIRS but higher than AHI and GOCI, and these patterns appeared more clearly when performance was analyzed by season. In addition, it was confirmed that the composite AOD model had more collocated pixels than the GEO or LEO satellites. Therefore, the composite AOD not only improved accuracy but helped compensate for the lack of aerosol information collected by the GEO satellites. Overall, the composite model acquired more aerosol information compared to the products of individual satellites.
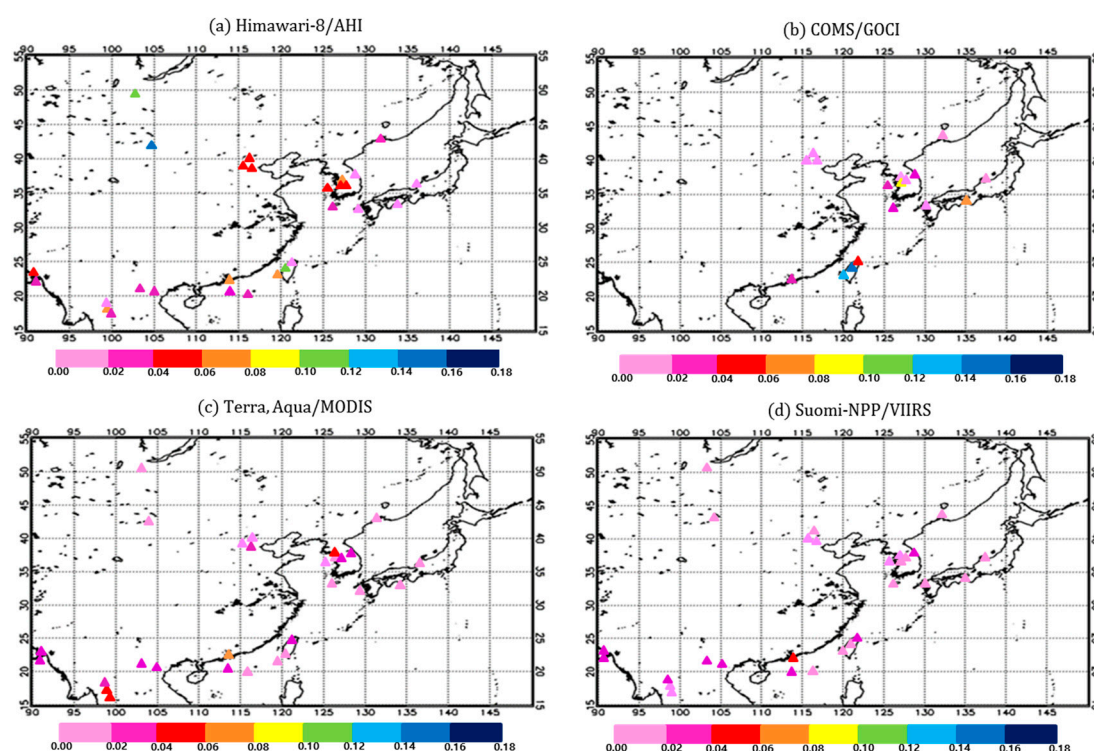

Figure 5. Statistical error (RMSE) analysis before and after applying a CDF comparing AERONET and satellite AOD values: (**a**) Himawari-8/AHI, (**b**) COMS/GOCI, (**c**) Aqua Terra/MODIS, and (**d**) Suomi-NPP/VIIRS.

3.2.2. Composite Spatial Variability and Satellite Retrieval Accuracy

The spatial variability of the modeled composite and the accuracy of satellite AOD products were explored at regional scales. In recent years, many Asian cities have suffered severe deterioration in air quality, with significant contributions from both natural and anthropogenic particulate sources. In particular, due to combined influences of arid dust production, large urban populations, and increasing fossil fuel usage, the Northeast Asian region often experiences very high concentrations of tropospheric aerosols. The resulting aerosols of Northeast Asia consist of a complex mixture of coarse and fine particulates, with both light-absorbing and scattering characteristics [49], so comparing local AOD concentrations is critical to know the main causes and sources of aerosols in different regions and to address them accordingly. In this study, regions were divided into Korea (Anmyondo, Gangneung_WNU, Seoul-University, Yonsei-University), China (Beijing, XiangHe), Japan (Fukuoka, Noto), and Taiwan (Chiang_Mai, Dahka-university, Dalanzadgad, Dongsha, EPA, Hongkong_PolyU, Taipei). Focusing on these fifteen AERONET sites, Figure A2 and Table A6 summarize the regional variations of composite and satellite AOD retrieval accuracy. The composite AOD performed better over China than Korea or Taiwan,

with a higher slope, lower intercept and a standard deviation very close to that of the AERONET data. Moreover, the composite AOD had a greater number of collocated sites over any single satellite and was vastly superior to that of GEO satellites in Taiwan region. Composite AOD values had a large number of collocations in China as well, suggesting that more aerosol information can be obtained by merging satellite data products than by single types of imagery. In China, R for the GEO satellites AHI and GOCI was 0.18 and 0.3, respectively, whereas this value in the composite increased to 0.75 from the inclusion of LEO satellite data (MODIS and VIIRS). The statistics show that AHI AOD values were significantly underestimated when aerosol loading was high, and slightly overestimated when aerosol loading was low. The decreased accuracy of AHI is likely attributable to the combined effects of complex effects of surface characterization and cloud contamination, resulting in a diminished retrieval quality. Moreover, the GOCI AOD values showed similar results to AHI AOD. On the other hand, the VIIRS AOD products performed slightly better over China and Korea than Japan and Taiwan. The R value for VIIRS AOD was the highest observed among the satellite-based AODs. The slopes and intercepts of the linear regression were 0.99 and 0.02, respectively, supporting what can be seen visually where VIIRS underestimates certain high-AOD events, and overestimates relatively low-AOD conditions. Moreover, the MODIS AOD showed a similar trend to VIIRS, but the accuracy was low.

3.2.3. Case Studies: Composite Accuracy and Air Pollution Source Tracking

Dust storms in the deserts of Northeast Asia can cause major aerosol events, spreading beyond the continental borders [110]. After applying the coefficients derived from the 2016 training dataset to each satellite, the composite field was calculated and analyzed for representative cases of these "yellow dust events" occurring in 2017.

Case 1: 18–19 April 2017

On 16–17 April 2017, two intense dust storms were generated over the Gobi Desert, Inner Mongolia, by springtime low pressure fronts descending from the northwest. After originating in the Gobi Desert, the dust storm shifted to the Loess plateau, impacting the southwestern part of the Korean peninsula during the afternoon of 17 April. The second dust storm was similarly generated over Inner Mongolia, and traveled through northeast China, affecting the whole Korean Peninsula on 18–19 April. The 72-h (three day) back trajectories were selected because it was deemed sufficient to determine the probable locations of regional emission sources and explain regional transport pathways [111–114]. Indeed, Figure 6k shows that nearly all of the HYSPLIT modeled trajectories originated from East China on 15–17 April; in particular, most of the modeled trajectories originated from Shanghai and Nanjing, while a portion had their beginnings in Inner Mongolia on 18–19 April. Figure 6a–j displays the hourly composite AOD for the 18 April case study. Figure 6a presents the hourly composite AOD with only GEO (i.e., AHI, GOCI) satellite retrievals, while Figure 6b utilized both GEO and Terra/MODIS satellite data. Figure 6c,d presents the hourly composite AOD with only GEO data. Figure 6e is an example of the 04:00 UTC composite utilizing all GEO and LEO (including Suomi-NPP/VIIRS) data examined. When producing the composite AOD field, LEO AOD values were merged with MODIS, VIIRS product derived from observations passing over Northeast Asia. Since only the GEO AOD values are available from 05:00 to 07:00 UTC, the composite AOD field is produced by combining the AHI and GOCI products (Figure 6f–h). As the GOCI observation is scheduled up to 07:00 UTC, only AHI AOD corrected by CDF fitting method is used from 08:00 to 09:00 UTC (Figure 6i,j). The GEO coverage has better spatial resolution, thus introducing GEO sensors into the composite AOD maps lead to considerable increases in spatial coverage. The greatest number of satellites are blended for the composite at 04:00 UTC (Figure 6e), which was able to obtain aerosol information from the Northeast China through with the inclusion of previously unobservable regions using a single GEO source. It is important to note that the composited GEO and LEO satellite retrievals used for Figure 6b,e merged rather well due to the overall good agreement in the spatial patterns

of GEO AOD values; therefore, the composited AOD field provided more detailed information on yellow dust events than any of its components could alone, offering a greater opportunity to understand flow patterns which can further help to monitor and model aerosol plumes.

Figure 6. Hourly composites of AOD from 00:00–09:00 UTC on 18 April 2017, and a three day back trajectory of the HYSPLIT Model: (**a**) 00:00 UTC, (**b**) 01:00 UTC, (**c**) 02:00 UTC, (**d**) 03:00 UTC, (**e**) 04:00 UTC, (**f**) 05:00 UTC, (**g**) 06:00 UTC, (**h**) 07:00 UTC, (**i**) 08:00 UTC, (**j**) 09:00 UTC, and (**k**) HYSPLIT on 15 (orange), 16 (purple), 17 (blue), 18 (light green), and 19 (green), April.

Case 2: 5–6 May 2017

The events of 5–6 May 2017 were chosen owing to the high AOD levels recorded at the regional background stations of the Korean Peninsula. The dust storm originated in eastern Mongolia and moved towards Korea. In particular, the northern part of the Korean Peninsula was affected by significant cloud cover, and the concentration of AOD > 2 on 4 May. In addition, the dust force was strengthened when the pressure trough developed from the low atmospheric pressure and front. Clouds in northern China prevented the sensors from collecting imagery, but AOD levels were high and arc-shaped along the cloud edge.

Figure 7 displays the hourly composite AOD acquired through the same process as in Case 1 (Section 3.2.3). The AOD values from AHI and GOCI (Figure 7a,c,d,f–h) were blended to contain spatial aerosol information from Northeast Asia as well. Moreover, it was possible to acquire additional information over the ocean by including LEO AOD products (Figure 7b,e). Compared to other times, the largest spatial coverage of aerosol information was obtained at 04:00 UTC (Figure 7e), when VIIRS data was included. The composite data from the Manchurian province on 5 May confirmed the aerosol concentration and proved useful to track the movement of the yellow dust event.
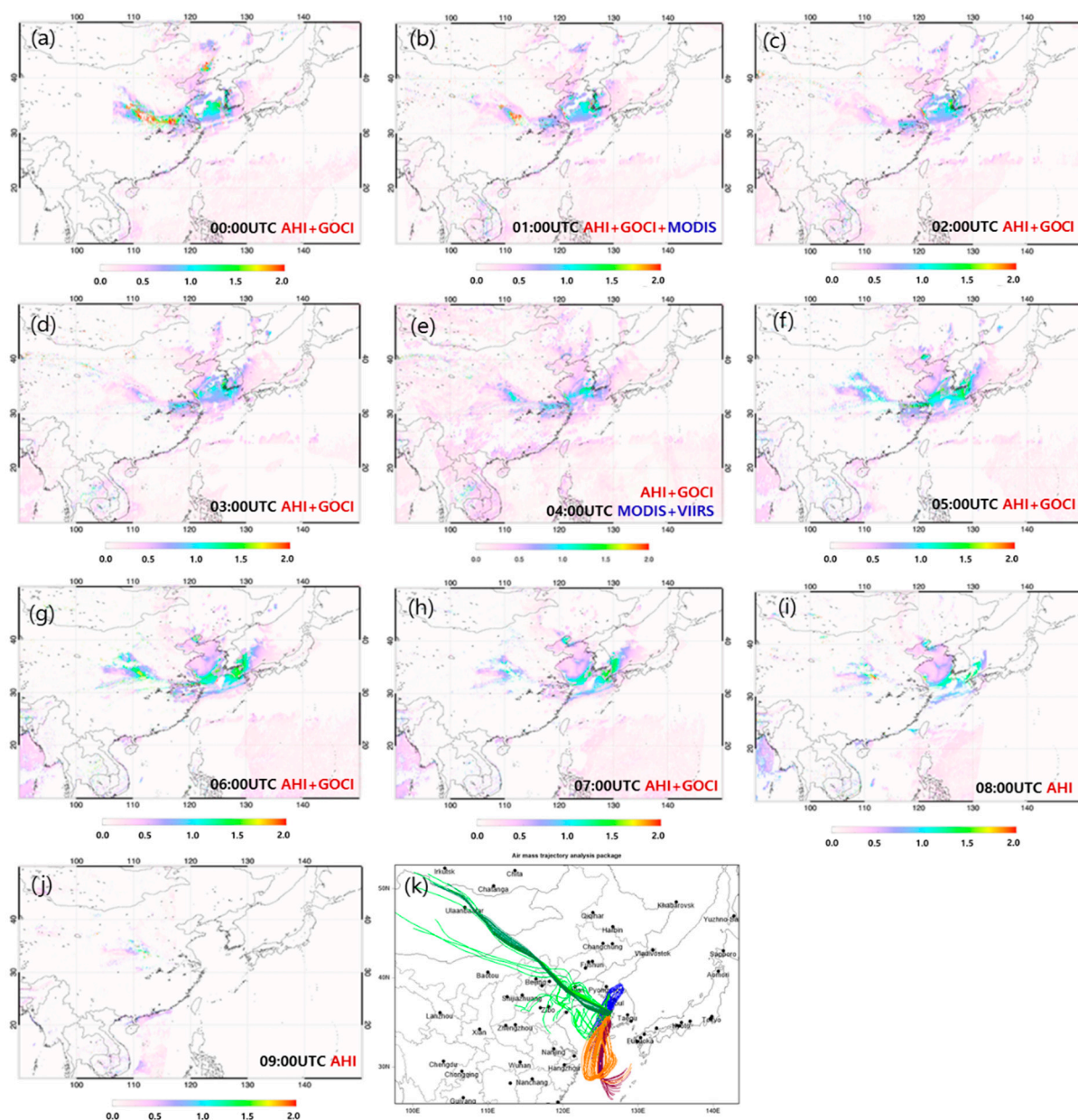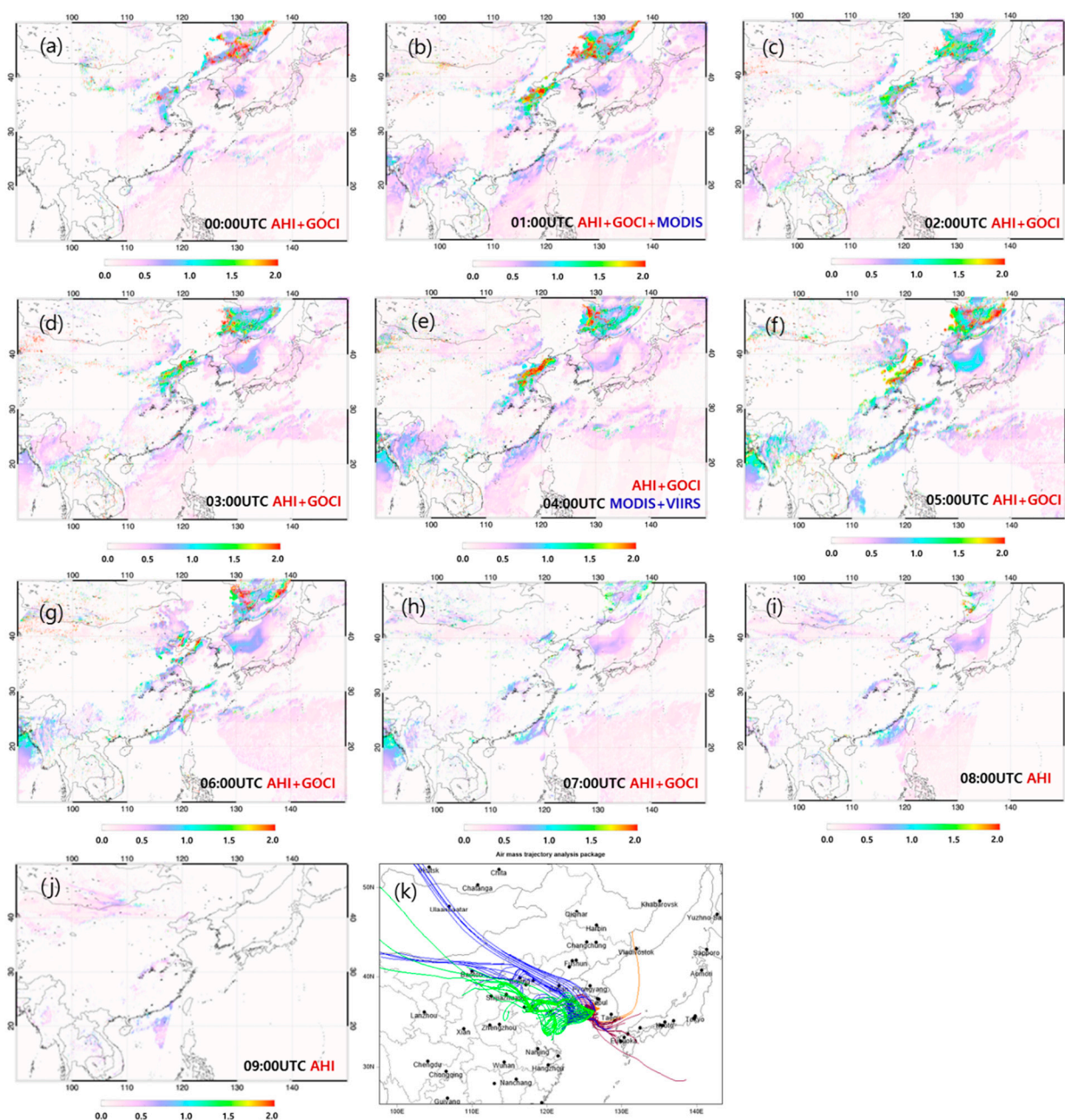

Figure 7. Hourly composites of AOD from 00:00–09:00 UTC on 5 May 2017, and a three day back trajectory of the HYSPLIT Model: (**a**) 00:00 UTC, (**b**) 01:00 UTC, (**c**) 02:00 UTC, (**d**) 03:00 UTC, (**e**) 04:00 UTC, (**f**) 05:00 UTC, (**g**) 06:00 UTC, (**h**) 07:00 UTC, (**i**) 08:00 UTC, (**j**) 09:00 UTC, and (**k**) HYSPLIT on 3 (orange), 4 (purple), 5 (blue), and 6 (light green), May.

Specifically, on 5 May, yellow dust spread widely throughout Southeast Asia, affecting all areas of the Korean Peninsula with relatively low AOD levels between 0.5 and 1.

Additionally, aerosols that had stalled in southeastern China for two days impacted the Korean Peninsula as they joined the northwest dust storm winds. The composite AOD also was able to identify high AOD at Shanghai and Nanjing in southeastern China, with the aerosol flow pattern gaining detail over time (Figure 7a–j). The HYSPLIT model's 72 h back trajectories (Figure 7k) on 3–4 May revealed that the air mass was stalled, and the high-pressure state lasted a significant period time. When high pressure remained stationary, ground-level air flow was mainly controlled by local circulation, providing optimal conditions for the accumulation of air pollutants [111]. It was also found that the high aerosol conditions observed in the Korean Peninsula originated from natural and anthropogenic sources. Therefore, when either yellow or fine dust events occur, the composited AOD offers greater information on aerosols and can be used for aerosol tracking and detailed monitoring along with air trajectory information.

3.3. Long-Term Accuracy of AOD Composite
3.3.1. Evaluation of Composite and Satellite AOD

The comparisons of composite and satellite information with AERONET AOD values at 500 nm for 15 sites in Northeast Asia over 2017 are presented in Figure 8. To validate the data, we calculated the average of all available AERONET AOD retrieval data for each site during the hourly observation periods of the composite. The nearest-neighbors approach was then employed to find the closest composite grid to each AERONET site. To investigate the influence of each satellite AOD product on the merged AOD accuracy, statistical metrics were compared. Figure 8d,e, presents R, RMSE, and MB for VIIRS (0.75, 0.23, and 0.084, respectively) and for MODIS (0.69, 0.28, and 0.11, respectively). The high R values indicate a strong correlation with AERONET data, as does the low bias compared to the slope of the linear regression. Additionally, as aerosol loading increased (AOD > 1), the values closed in on the one-to-one line, indicating that LEO satellites are superior at detecting high aerosol concentration plumes. Alternatively, R, RMSE, and MB for the AHI data (Figure 8b) were 0.28, 0.39, and 0.105, respectively; and GOCI data (Figure 8c) produced values of 0.39, 0.36, and 0.096, respectively. Thus, the results for GEO satellites showed a poor correlation with AERONET data, and the hourly composites including only GEO contained the greatest level of uncertainty [115]. The strength of underestimation of the composite gradually increased with greater aerosol concentrations, likely a result of inaccurate characterization of surface reflectance and inadequate representation of the aerosol model [116]; however, the composite AOD achieved a relatively moderate agreement with AERONET measurements (Figure 8e). Additionally, the composite improved LEO overestimation from 0 < AOD < 0.5, and GEO underestimation AOD > 0.5. Moreover, it increased the number of collocations. It was thus concluded that the composite AOD values are strongly dependent on the accuracy of LEO satellite products and the number of GEO pixels.

3.3.2. Regional Composite and Satellites Retrieval Accuracy

Statistical parameters of the composite, MODIS, VIIRS, AHI, and GOCI AOD products are delineated by AERONET sites in Table 4. These validation results show that the collocation pixel number in the composite products was consistently greater than any individual satellite's product, supporting the value of composite creation; however, the composite showed variable statistical parameters across regions. For example, the composite over the Noto, Japan, site had the smallest MB and RMSE compared with the Korean Peninsula and Chinese sites. In particular, composite RMSE was lower than that of MODIS but not VIIRS. The composite over the Gangneung, Korean site, had the second smallest MB and RMSE, and the collocation number of datapoints was the highest. This site was the most reliably estimated by AHI and occupies the largest area, with a lower RMSE and higher accuracy than other regions. The results over the Taipei site in South China had the third smallest MB and RMSE, primarily driven by the high accuracy of MODIS and VIIRS. Next, the results from Yonsei University site in Korea had the fourth smallest MB, RMSE, and collocation

number, indicating that the number of collocations was increased by the GEO satellites and further reflected the high accuracy of MODIS and VIIRS.
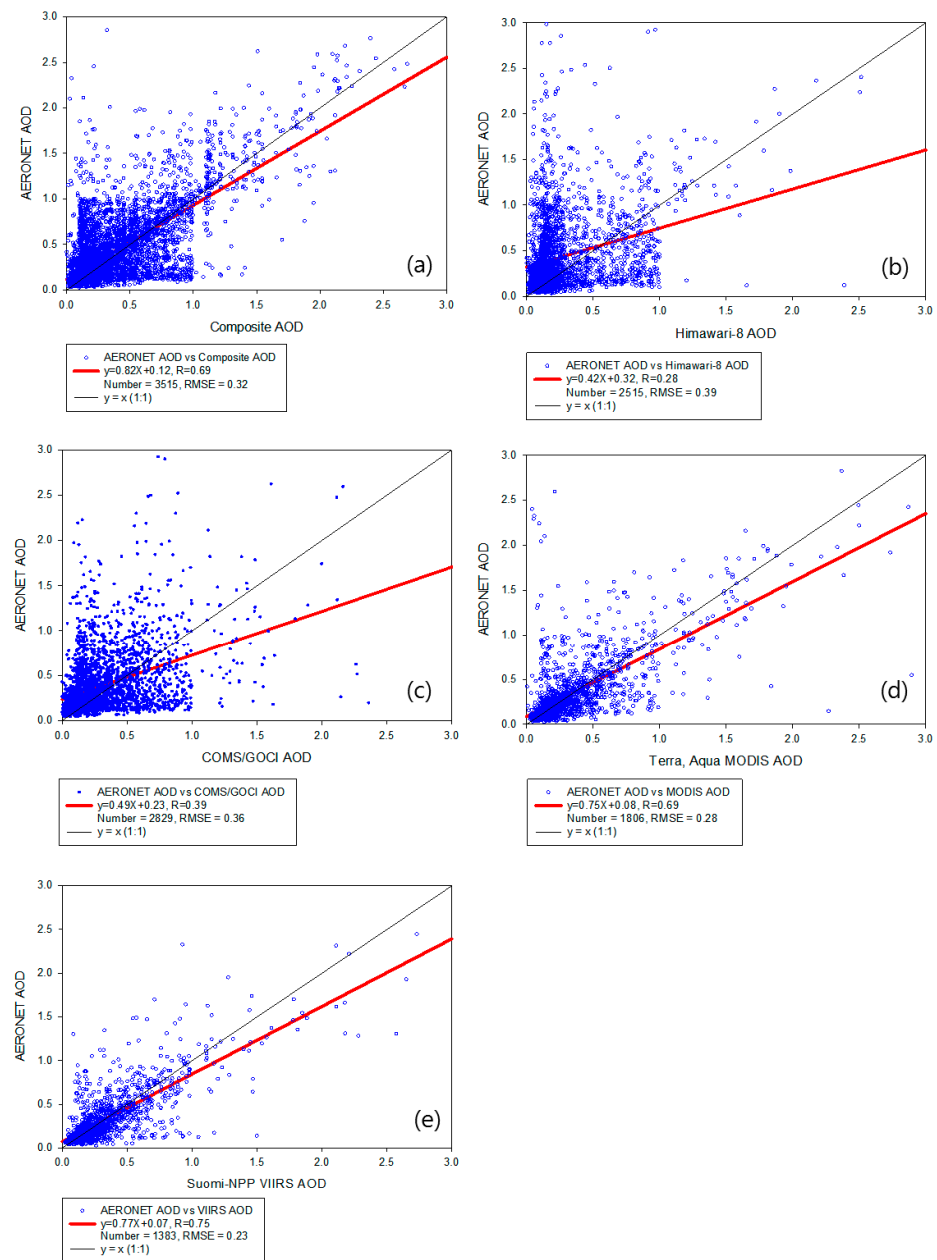

Figure 8. AOD scatterplots from (**a**) Composite, (**b**) Himawari-8/AHI, (**c**) COMS/GOCI, (**d**) Aqua Terra/MODIS, and (**e**) Suomi-NPP/VIIRS against ground-based reference AERONET data for 15 sites from January to December 2017. Solid red line is the linear regression, and the black line is 1:1.

Table 4. Summary statistics for composite, satellites, and AERONET AOD products during 2017.

Satellite	Site	AERONET	Composite	AHI	GOCI	MODIS	VIIRS
Bias		-	0.036	0.054	0.124	0.120	0.095
RMSE		-	0.191	0.232	0.353	0.171	0.208
Collocation-number	Anmyon	959	636	226	335	146	148
Linear regression slope		-	y = 0.615x + 0.088	y = 0.356x + 0.025	y = 0.601x + 0.084	y = 0.714x + 0.076	y = 0.752x + 0.117
R (correlation coefficient)		-	0.697	0.353	0.499	0.777	0.807
Bias		-	0.156	0.138	0.189	0.010	0.011
RMSE		-	0.325	0.372	0.435	0.104	0.105
Collocation-number	Beijing	1320	763	280	318	180	131
Linear regression slope		-	y = 0.731x + 0.084	y = 0.156x + 0.242	y = 0.189x + 0.330	y = 0.908x + 0.093	y = 0.970x + 0.003
R (correlation coefficient)		-	0.698	0.253	0.268	0.791	0.841
Bias		-	0.172	0.221	-	0.216	0.216
RMSE		-	0.215	0.269	-	0.265	0.264
Collocation-number	Chiang_Mai_Met_Sta	1550	730	480	-	135	120
Linear regression slope		-	y = 0.431x + 0.183	y = 0.479x + 0.134	-	y = 0.415x + 0.201	y = 0.401x + 0.186
R (correlation coefficient)		-	0.458	0.385	-	0.447	0.402
Bias		-	0.139	0.158	-	0.151	0.150
RMSE		-	0.273	0.298	-	0.290	0.187
Collocation-number	Dalanzadgad	1598	682	300	-	249	103
Linear regression slope		-	y = 0.648x + 0.112	y = 0.221x + 0.104	-	y = 0.696x + 0.304	y = 0.717x + 0.097
R (correlation coefficient)		-	0.658	0.387	-	0.676	0.754
Bias		-	0.214	0.301	-	0.266	0.279
RMSE		-	0.263	0.248	-	0.216	0.228
Collocation-number	Dhaka-University	741	307	191	-	96	56
Linear regression slope			y = 0.585x + 0.134	y = 0.196x + 0.171	-	y = 0.499x + 0.270	y = 0.270x + 0.304
R (correlation coefficient)			0.638	0.322	-	0.653	0.692

Table 4. *Cont.*

Satellite	Site	AERONET	Composite	AHI	GOCI	MODIS	VIIRS
Bias		-	0.193	0.195	-	0.192	0.191
RMSE		-	0.220	0.241	-	0.238	0.237
Collocation-number	Dongsha-Island	513	165	106	-	100	114
Linear regression slope			y = 0.615x + 0.090	y = 0.360 + 0.016	-	y = 0.632x + 0.179	y = 0.663x + 0.050
R (correlation coefficient)			0.763	0.396	-	0.641	0.690
Bias		-	0.047	0.059	-	0.014	0.043
RMSE		-	0.201	0.243	-	0.203	0.207
Collocation-number	EPA-NCU	573	171	136	-	65	67
Linear regression slope			y = 0.579x + 0.117	y = 0.263 + 0.139	-	y = 0.617x + 0.159	y = 0.706x + 0.154
R (correlation coefficient)			0.632	0.193	-	0.630	0.689
Bias		-	0.065	0.027	0.065	0.065	0.010
RMSE		-	0.254	0.164	0.255	0.255	0.103
Collocation-number	Fukuoka	874	479	173	329	83	55
Linear regression slope			y = 0.531x + 0.155	y = 0.266x + 0.141	y = 0.301x + 0.184	y = 0.517x + 0.159	y = 0.708x + 0.154
R (correlation coefficient)			0.529	0.195	0.359	0.529	0.689
Bias		-	0.149	0.057	0.095	0.095	0.095
RMSE		-	0.126	0.139	0.208	0.208	0.208
Collocation-number	Gang neung	1556	638	471	574	180	157
Linear regression slope			y = 0.659x + 0.072	y = 0.091x + 0.210	y = 0.210x + 0.211	y = 0.639x + 0.159	y = 0.680x + 0.065
R (correlation coefficient)			0.677	0.125	0.233	0.640	0.696
Bias		-	0.045	0.060	-	0.010	0.011
RMSE		-	0.212	0.246	-	0.104	0.105
Collocation-number	Hongkong PolyU	115	222	204	-	107	87
Linear regression slope			y = 0.851x + 0.001	y = 0.214 + 0.179	-	y = 0.789x + 0.051	y = 0.801x + 0.081
R (correlation coefficient)			0.800	0.446	-	0.942	0.952

Table 4. *Cont.*

Satellite	Site	AERONET	Composite	AHI	GOCI	MODIS	VIIRS
Bias		-	0.014	0.031	0.045	0.031	0.002
RMSE		-	0.120	0.175	0.213	0.176	0.047
Collocation-number	Noto	318	314	129	282	126	111
Linear regression slope			y = 0.681x + 0.172	y = 0.105x + 0.104	y = 0.205x + 0.201	y = 0.713x + 0.097	y = 0.760x + 0.599
R (correlation coefficient)			0.787	0.218	0.228	0.770	0.788
Bias		-	0.183	0.053	0.124	0.122	0.035
RMSE		-	0.229	0.229	0.252	0.249	0.188
Collocation-number	Seoul-University	1500	767	212	589	266	224
Linear regression slope			y = 0.625x + 0.154	y = 0.200x + 0.214	y = 0.418x + 0.195	y = 0.741x + 0.143	y = 0.802x + 0.106
R (correlation coefficient)			0.693	0.249	0.440	0.687	0.714
Bias		-	0.057	0.0452	-	0.013	0.014
RMSE		-	0.138	0.212	-	0.116	0.118
Collocation-number	Taipei_CWB	895	331	258	-	81	90
Linear regression slope			y = 0.643x + 0.178	y = 0.205 + 0.311	-	y = 0.683x + 0.193	y = 0.649x + 0.211
R (correlation coefficient)			0.683	0.313	-	0.696	0.647
Bias		-	0.246	0.078	0.124	0.120	0.042
RMSE		-	0.296	0.279	0.352	0.247	0.204
Collocation-number	XiangHe	1602	550	277	362	176	257
Linear regression slope			y = 0.606x + 0.099	y = 0.300x + 0.111	y = 0.338x + 0.207	y = 0.857x + 0.388	y = 1.089x + 0.037
R (correlation coefficient)			0.722	0.328	0.444	0.844	0.863
Bias		-	0.126	0.115	0.129	0.120	0.038
RMSE		-	0.154	0.238	0.259	0.147	0.195
Collocation-number	Yonsei-University	1552	634	488	627	184	164
Linear regression slope			y = 0.595x + 0.022	y = 0.401x + 0.021	y = 0.432x + 0.032	y = 0.811x + 0.211	y = 0.901x + 0.051
R (correlation coefficient)			0.68	0.411	0.488	0.811	0.877

In summary, estimates for 12 sites of the 15 AERONET sites were improved by the accuracy of the composite AOD: 7 sites were affected by MODIS accuracy (Anmyondo, Beijing, Dhaka-university, EPA-NCU, Hongkong_PolyU, Taipei, and Yonsei-university), and the other 5 sites were positively affected by the accuracy of VIIRS (Dalanzadgad, Fukuoka, Noto, Seoul-university, and XiangHe). Ultimately the accuracy of LEO AOD values is reflected in the composite, but it is not always possible to attain the same level accuracy when merging all data sources. Although sometimes less accurate than the individual LEO AODs, it is expected that the use of composite AOD will be superior because it improves RMSE and bias over single image GEO AODs. However, the least accurate composite AOD sites were Chinese, including Beijing and XiangHe, where RMSE and bias remained high even after CDF fitting. Overall, this validation result showed that the accuracy of the composite AOD improved from the inclusion of the influence of LEO AOD products, and the number of data sites increased from the inclusion of GEO AOD products.

3.3.3. Composite AOD Accuracy Assessment

To validate the composite AOD values and compare them with the accuracy of original AHI, GOCI, MODIS, and VIIRS AODs, all satellite and composite AOD data were spatiotemporally collocated with AERONET AOD site measurements. The satellite and composite AOD products were averaged over 10 km × 10 km (0.1°) regions, centered on each AERONET site. Correspondingly, the AERONET AOD data was averaged within ±1 h of the time each satellite passed over the site. Figure 9 depicts the correlation and histogram, as well as the scatter plots between AERONET and satellite AODs at AERONET sites during 2017. The GEO satellite correlation coefficients indicated an underestimation of AERONET data, mostly allocated from 0.0 to 1.0 in the histogram distribution. Alternatively, the LEO satellites showed consistent accuracy when compared to AERONET site data, and although the composite AOD developed in this study showed better correlation than GEOs, the accuracy of LEO satellites was unmatched. Additionally, VIIRS is a heritage of MODIS, showing a high correlation coefficient, confirming the similar characteristics of their AOD algorithms. It should be noted that the composite AOD showed good correlation with MODIS and VIIRS, as well as a similar histogram distribution. In other words, it can be confirmed that the high accuracy of the LEO satellites, and the high spatial resolution of their orbit are reflected in the composite AOD. This is also evident in the analysis of the deviation between AERONET, composite and individual satellite data (Figure 10). Most satellite AOD products tended to overestimate AERONET measurements, especially in 2017. The composite AOD developed in this study applied the CDF method to reduce the error for each satellite and showed a good ability to reduce deviation. In particular, when compared with other satellite AOD values, the composite showed a negative deviation that was alleviated from January to June 2017, and near zero deviation from July to December, indicating higher overall accuracy. Overall, the statistics suggest that the composite AOD yielded a highly similar standard deviation to AERONET measurements and outperformed the GEO satellites. This study has great significance in that the data of the aerosol optical thickness (L2) of each satellite were blended using CDF, a statistical method rather than a physical method. By reducing the uncertainty of each satellite's AOD algorithm as much as possible and simply calculating it using statistical techniques, we have developed an algorithm that can not only obtain a large amount of geostationary orbit information but also reflect the high accuracy of polar orbit satellites.

3.3.4. Limitations of Composite AOD

Extensive ground-based monitoring networks exist in some parts of the world, but major portions of the globe remain unmonitored [13]; thus, due to the lack of observation points, and satellite image using the CDF method is hindered by spatial limitations. Northeast Asia is a large region, and coverage of the AERONET sites is likely insufficient to adequately monitor and model the entire area. The CDF fitting method used in this study

forcibly reproduced the coefficients attained from the 27 AERONET stations; therefore, it induced error because it was calculated assuming a non-AERONET site location. Additionally, ocean and offshore areas were corrected to a value close to zero since marine areas far from land are not included due to the absence of AERONET stations (limitations on the method). Second, in this study, we also produced the composite using Level 2 of satellite AODs, exhibiting differences in satellite-based product retrieval algorithms, spatial and temporal resolutions, sampling, radiometric calibration, and cloud-screening mechanisms. The use of the aerosol retrievals from single satellite sensors alone can contain incomplete aerosol spatial distributions due to cloud cover, sun glint, and sensor limitations (e.g., spatial resolution, scan coverage) [117]. Particularly, it is difficult to distinguish aerosols above highly reflective surfaces; for example, MODIS AOD can be retrieved except in highly uncertain locations (cloudy regions, snow/ice, desert areas). Since the Level 2 product of aerosols was calculated for each satellite except over cloud regions (cloud, shallow layer of pollution), the aerosol column may not be observable, even if aerosol concentration is dense in the clouded area (limitations on the data).
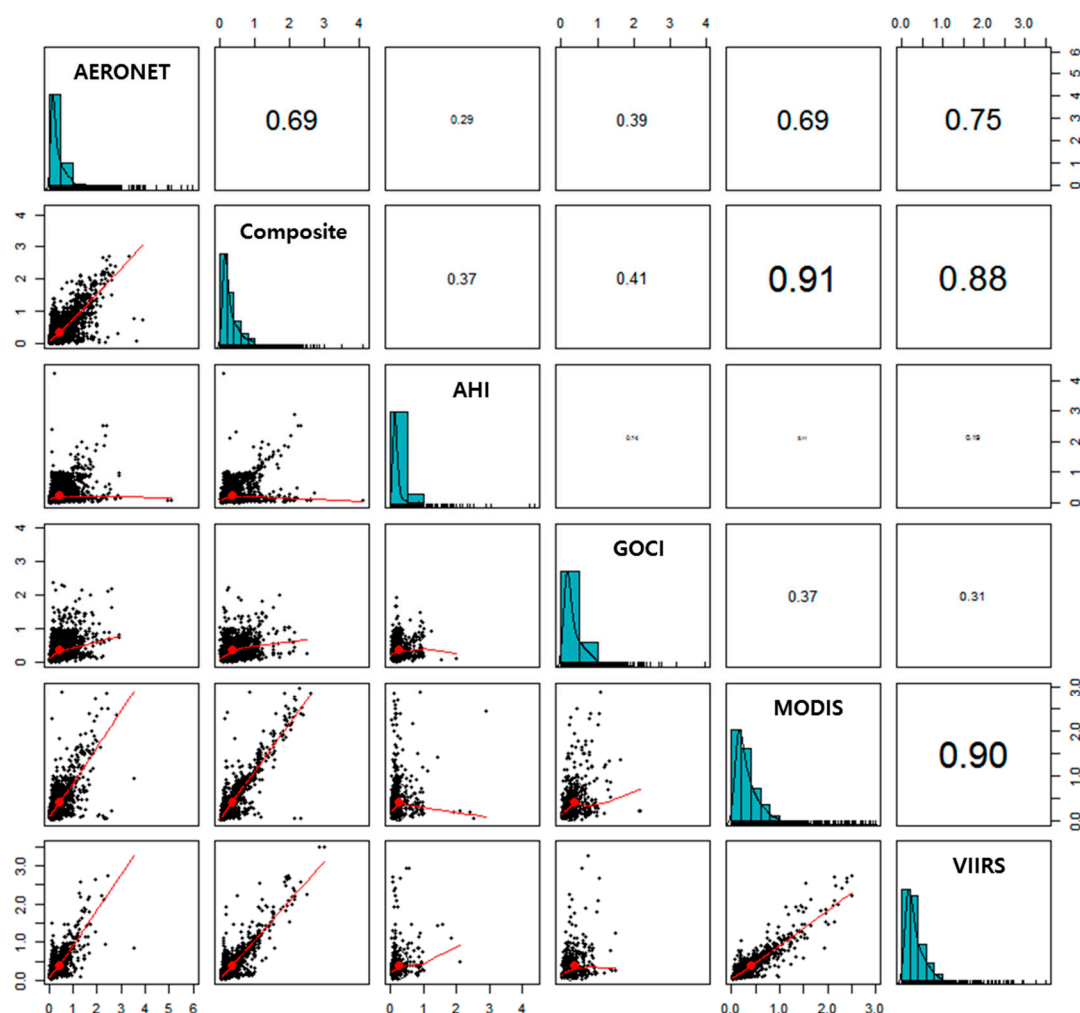

Figure 9. Bivariate Pearson correlation coefficients (r) between pairs of AERONET vs. composite and satellite data across Northeast Asia during 2017. Numerical values above the diagonal are linear correlation coefficients; scatter plots below the diagonal are of paired variables fit with a non-linear parametric smoothing function.
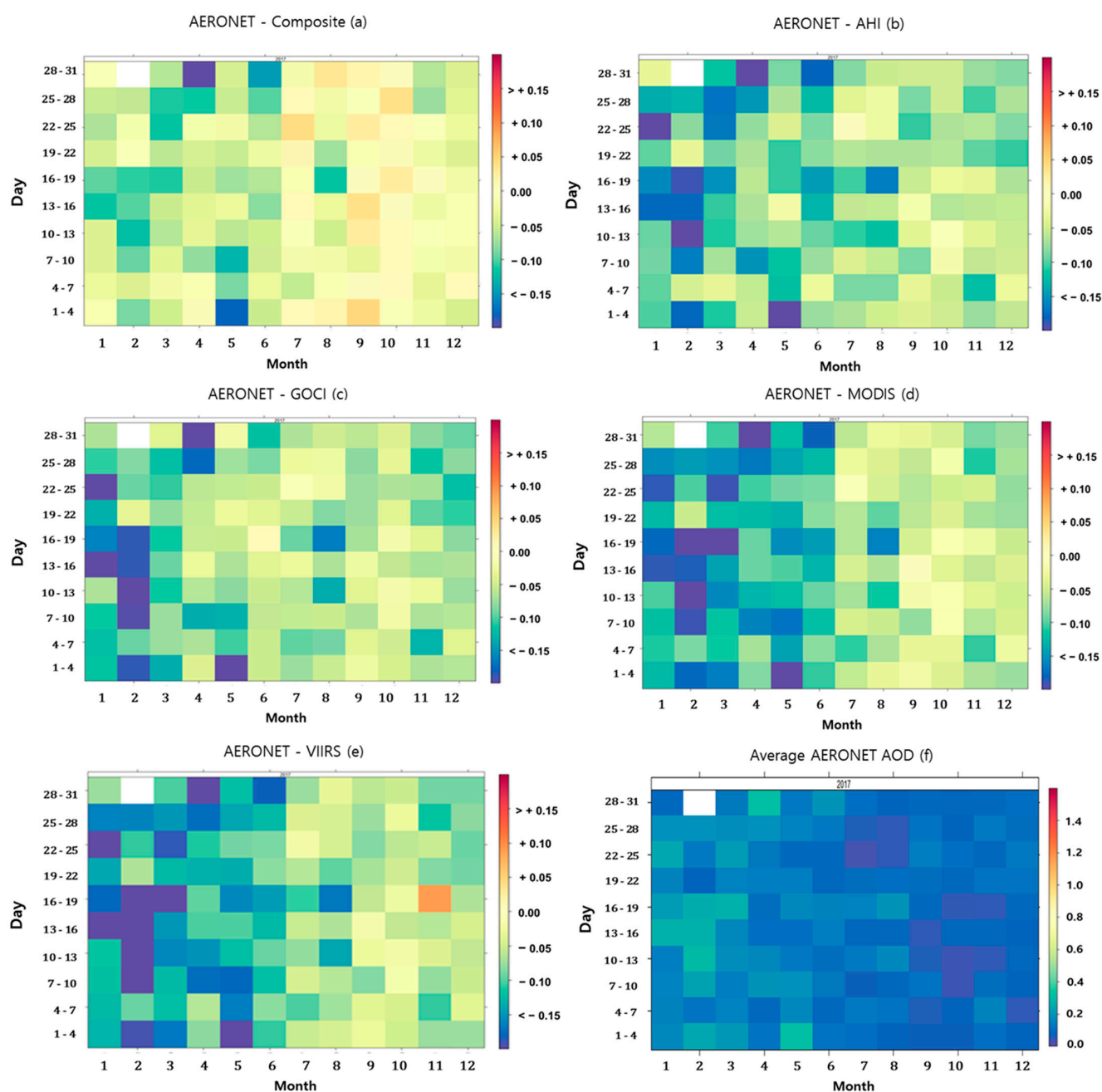
Figure 10. Seasonal and diurnal mean deviation of AOD between AEORNET, composite, and satellite data during 2017: (**a**) Composite, (**b**) Himawari-8/AHI, (**c**) COMS/GOCI, (**d**) Aqua Terra/MODIS, and (**e**) Suomi-NPP/VIIRS (**f**) AERONET Average AOD.

4. Summary and Conclusions

The primary goal of this study was to generate hourly composite AOD products that combined GEO and LEO satellite observations, to assist with monitoring the transport of aerosol plumes over Northeast Asia. A methodology was developed to rescale and merge GEO and LEO retrievals and produce an improved AOD dataset. Hourly AOD composites were generated that achieved a wider spatial coverage of AOD domain in Northeast Asia. The composited AOD results indicated that (a) although the inclusion of GEO satellite products degraded the accuracy, the composite was improved in terms of the spatiotemporal resolution of the data; (b) despite the relative infrequency of LEO data acquisition, the composite AOD accuracy was increased according to the error metrics

(i.e., R, RMSE, MB, and MAE) and indicated a stronger performance; and (c) the composite AOD often provided the most aerosol information, supporting that when GEO and LEO satellite products are rescaled, composite products can offer enhanced AOD data over Northeast Asia. The complementary features of the AOD products derived from different satellite sensors in terms of their spatial completion and accuracy made it possible to produce improved AOD hourly products by merging multisensory satellite products. Moreover, these products can assist with tracking and modeling the transport of aerosols over Northeast Asia.

Although the composite AOD product increased spatial coverage, several issues were noted pertaining to the AOD retrievals. The results showed that the composite AOD estimates can appear in the ocean due to cloud artifacts impacting GEO and LEO satellite retrievals when the CDF matching method was applied. The methodology developed here was also dependent on the availability of the data being composited, and gaps in space or time may lead to inaccurate estimates of composite AOD distribution. However, the data fusion approaches for acquiring new data with higher accuracy and temporal and spatial resolution are encouraged.

The future capability of GEO satellites for monitoring and tracking aerosol plumes will be enhanced with the GEO-KOMPSAT 2A (GK-2A) satellite launched in December of 2018. The GK-2A can perform full disk scans every 10 min and carries the Advanced Meteorological Imager (AMI) consisting of 16 spectral bands between 400–1330 nm. Hence, its much-improved spatial resolution (2 km) can further enhance the monitoring ability of aerosol plumes over the Northeast-Asia. It is expected that the high temporal resolution of GK-2A can lead to a more complete understanding of aerosol spatial distribution over Northeast Asia which prevented the damage by responding through aerosol forecasts such as yellow dust and fine dust. Moreover, it will be importantly used to study long-term climate change by collecting information on aerosols. Furthermore, the findings here will be utilized for the data assimilation of the Asia Dust Aerosol Model 3 (ADAM3) model operated by the Korea Meteorological Administration.

Author Contributions: Conceptualization, S.A. and S.-R.C.; methodology, S.A. and C.-Y.C.; software, S.A.; validation, S.A.; formal analysis, S.A.; investigation, S.A.; resources, S.A.; data curation, S.A.; writing—original draft preparation, S.A.; writing—review and editing, S.-R.C. and H.-J.O.; visualization, S.A.; supervision, S.-R.C.; project administration, S.-R.C.; All authors have read and agreed to the published version of the manuscript.

Institutional Review Board Statement: Not applicable.

Informed Consent Statement: Not applicable.

Data Availability Statement: Data available on request due to restrictions eg privacy or ethical. The data presented in this study are available on request from the corresponding author.

Conflicts of Interest: The authors declare no conflict of interest.

Abbreviations

ADAM3	Asian Dust Aerosol Model 3
AOD	aerosol optical depth
CDF	cumulative distribution function
EDR	environmental data record
GEO	geosynchronous equatorial orbit
ICW	inverse composite weighting
IDW	inverse distance weighting
LEO	low earth orbit

Appendix A

Figure A1. Seasonal comparison between AERONET and satellite AOD values for 2017: (**a**) Composite, (**b**) Himawari-8/AHI, (**c**) COMS/GOCI, (**d**) Aqua Terra/MODIS, and (**e**) Suomi-NPP/VIIRS. Blue line is the linear regression fit, and gray shading shows the associated error range.
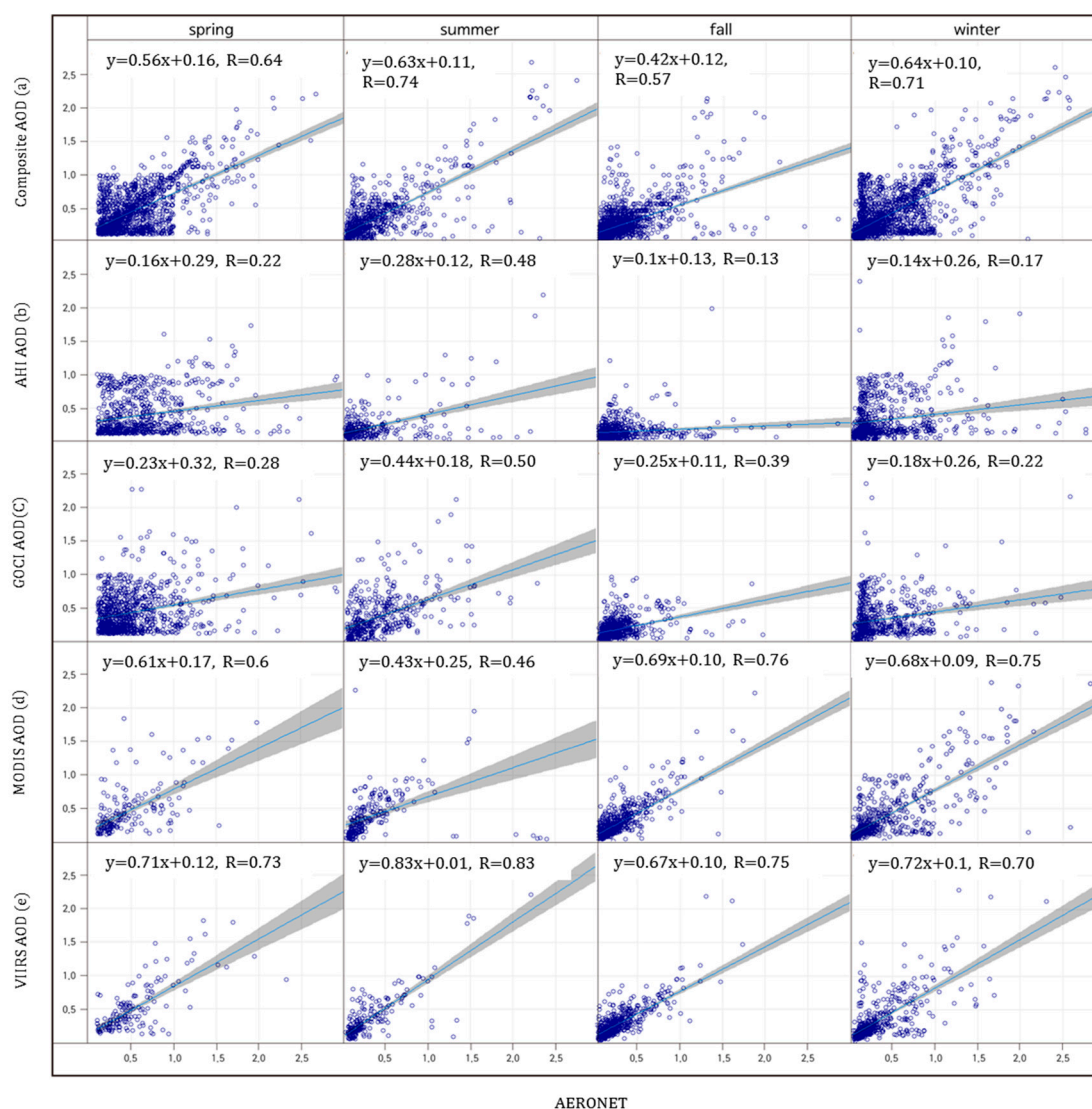
Figure A2. Regional comparison between AERONET and satellite AOD values for 2017: (**a**) Composite, (**b**) Himawari-8/AHI, (**c**) COMS/GOCI, (**d**) Aqua Terra/MODIS, and (**e**) Suomi-NPP/VIIRS. Blue line is the linear regression fit, and gray shading shows the associated error range.
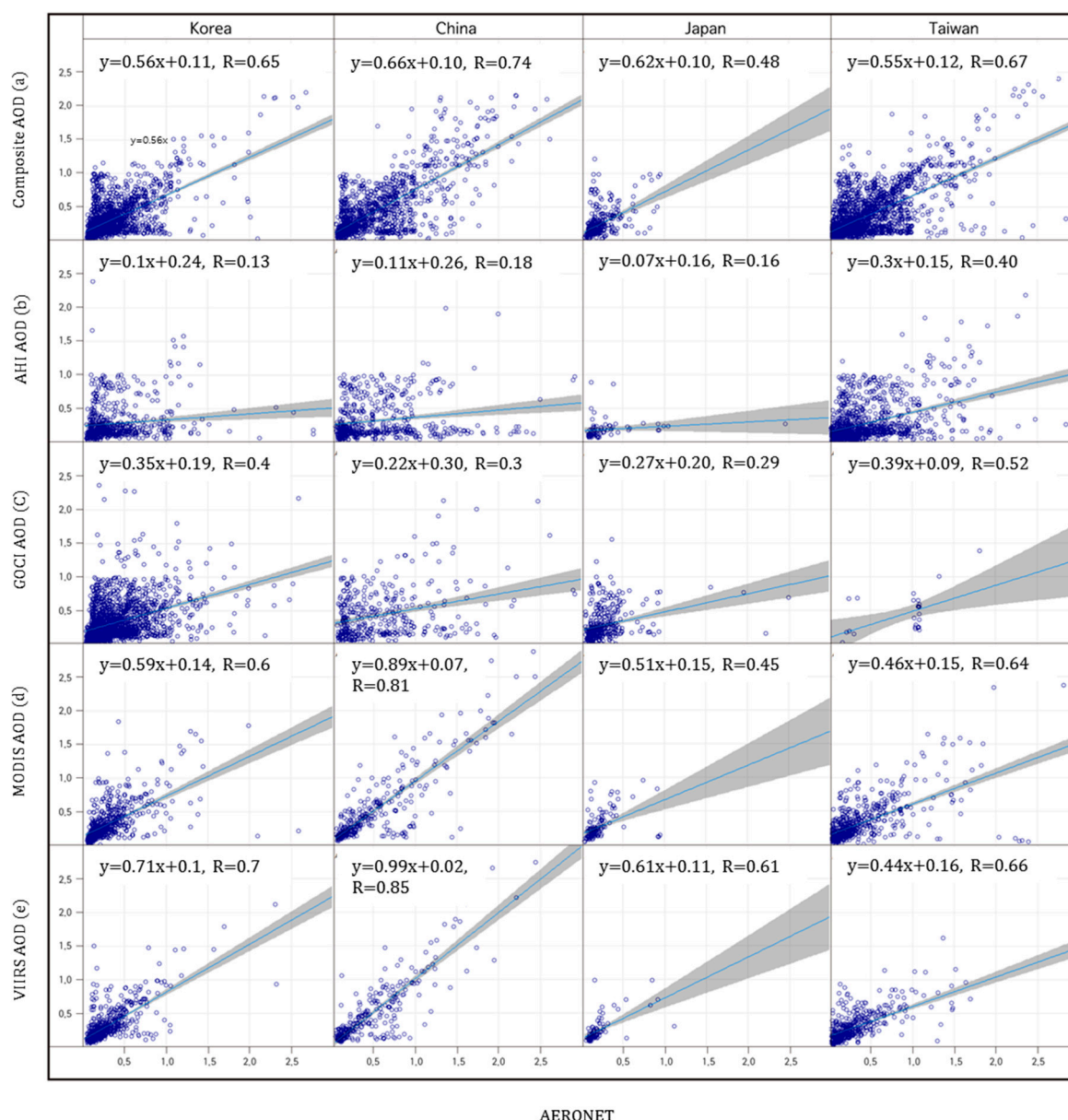
Table A1. Summary coefficients of Himawari-8/AHI AOD products during 2016 in training data ($X = AOD$).

AERONET Sites	Himawari-8 AHI	a_0	a_1	a_2	a_3
Anmyon	$a_0 + a_1 X + a_2 X^2 + a_3 X^3$	0.074	-0.133	0.007	0.018
Baengnyeong	$a_0 + a_1 X + a_2 X^2 + a_3 X^3$	0.026	-0.072	0.029	-0.119
Beijing-CAMS	$a_0 + a_1 X + a_2 X^2 + a_3 X^3$	0.035	-0.072	0.005	0.010
Beijing	$a_0 + a_1 X + a_2 X^2 + a_3 X^3$	0.148	-0.077	0.006	0.096
Bhola	$a_0 + a_1 X + a_2 X^2 + a_3 X^3$	0.096	-0.351	0.024	0.052
Chen−Kung_Univ.	$a_0 + a_1 X + a_2 X^2 + a_3 X^3$	0.128	0.023	-0.021	0.019
Chiang_Mai_Met_Sta	$a_0 + a_1 X + a_2 X^2 + a_3 X^3$	0.287	0.144	-0.043	0.015
Dalanzadgad	$a_0 + a_1 X + a_2 X^2 + a_3 X^3$	0.205	-0.051	-0.017	0.018
Dhaka−Univ.	$a_0 + a_1 X + a_2 X^2 + a_3 X^3$	0.331	-0.697	0.087	0.013
Dongsha_Island	$a_0 + a_1 X + a_2 X^2 + a_3 X^3$	0.001	-0.116	0.022	0.051
Doi_Ang−Khang	$a_0 + a_1 X + a_2 X^2 + a_3 X^3$	0.018	-0.118	-0.002	0.092

Table A1. *Cont.*

AERONET Sites	Himawari-8 AHI	a_0	a_1	a_2	a_3
EPA−NCU	$a_0 + a_1 X + a_2 X^2 + a_3 X^3$	0.002	−0.251	0.024	0.058
Fukuoka	$a_0 + a_1 X + a_2 X^2 + a_3 X^3$	0.061	−0.413	0.054	0.068
Gangneung_WNU	$a_0 + a_1 X + a_2 X^2 + a_3 X^3$	0.190	−0.268	0.022	0.045
Gosan_SNU	$a_0 + a_1 X + a_2 X^2 + a_3 X^3$	0.152	−0.334	0.045	−0.058
Hongkong_PolyU	$a_0 + a_1 X + a_2 X^2 + a_3 X^3$	0.156	−0.458	0.062	−0.083
Irkutsk	$a_0 + a_1 X + a_2 X^2 + a_3 X^3$	0.544	−0.012	−0.038	0.041
NGHIA_DO	$a_0 + a_1 X + a_2 X^2 + a_3 X^3$	0.055	−0.194	0.031	−0.033
Noto	$a_0 + a_1 X + a_2 X^2 + a_3 X^3$	0.043	−0.208	0.120	0.063
Omkoi	$a_0 + a_1 X + a_2 X^2 + a_3 X^3$	0.344	−0.375	0.038	0.101
Seoul_SNU	$a_0 + a_1 X + a_2 X^2 + a_3 X^3$	0.082	−0.541	0.081	0.082
Shirahama	$a_0 + a_1 X + a_2 X^2 + a_3 X^3$	0.044	−0.194	0.007	0.027
Son_La	$a_0 + a_1 X + a_2 X^2 + a_3 X^3$	0.091	−0.593	0.102	0.084
Taipei_CWB	$a_0 + a_1 X + a_2 X^2 + a_3 X^3$	0.023	−0.232	−0.004	0.019
Ussuriysk	$a_0 + a_1 X + a_2 X^2 + a_3 X^3$	0.038	−0.162	−0.014	0.012
XiangHe	$a_0 + a_1 X + a_2 X^2 + a_3 X^3$	0.004	0.061	−0.014	0.012
Yonsei_Univ.	$a_0 + a_1 X + a_2 X^2 + a_3 X^3$	0.096	−0.308	0.034	0.057

Table A2. Summary coefficients of COMS/GOCI AOD products during 2016 in training data ($X = AOD$).

AERONET Sites	COMS GOCI	a_0	a_1	a_2	a_3
Anmyon	$a_0 + a_1 X + a_2 X^2 + a_3 X^3$	0.074	2.703	0.003	0.000
Baengnyeong	$a_0 + a_1 X + a_2 X^2 + a_3 X^3$	0.143	0.044	0.013	0.109
Beijing-CAMS	$a_0 + a_1 X + a_2 X^2 + a_3 X^3$	0.044	0.735	0.021	0.003
Beijing	$a_0 + a_1 X + a_2 X^2 + a_3 X^3$	0.038	0.912	−0.025	1.010
Bhola					
Chen−Kung_Univ.					
Chiang_Mai_Met_Sta					
Dalanzadgad					
Dhaka−Univ.					
Dongsha_Island					
Doi_Ang−Khang					
EPA−NCU	$a_0 + a_1 X + a_2 X^2 + a_3 X^3$	0.012	1.296	−0.187	0.001
Fukuoka	$a_0 + a_1 X + a_2 X^2 + a_3 X^3$	−0.143	1.438	−0.147	0.001
Gangneung_WNU	$a_0 + a_1 X + a_2 X^2 + a_3 X^3$	0.058	0.477	0.570	0.001
Gosan_SNU	$a_0 + a_1 X + a_2 X^2 + a_3 X^3$	0.023	0.864	0.056	0.001
Hongkong_PolyU					
Irkutsk					
NGHIA_DO					
Noto	$a_0 + a_1 X + a_2 X^2 + a_3 X^3$	0.175	−0.191	0.021	−0.021
Omkoi					
Seoul_SNU	$a_0 + a_1 X + a_2 X^2 + a_3 X^3$	−0.049	0.838	−0.021	0.002
Shirahama	$a_0 + a_1 X + a_2 X^2 + a_3 X^3$	0.023	1.324	−0.431	0.001
Son_La					
Taipei_CWB	$a_0 + a_1 X + a_2 X^2 + a_3 X^3$	0.059	1.388	−0.290	0.001
Ussuriysk	$a_0 + a_1 X + a_2 X^2 + a_3 X^3$	0.034	0.793	−0.195	0.000
XiangHe	$a_0 + a_1 X + a_2 X^2 + a_3 X^3$	0.036	0.998	0.135	0.684
Yonsei_Univ.	$a_0 + a_1 X + a_2 X^2 + a_3 X^3$	0.034	0.900	0.059	1.051

Table A3. Summary coefficients of Terra, Aqua/MODIS AOD products during 2016 in training data ($X = AOD$).

AERONET Sites	Terra, Aqua MODIS	a_0	a_1	a_2	a_3
Anmyon	$a_0 + a_1 X + a_2 X^2 + a_3 X^3$	0.074	2.703	0.003	0.000
Baengnyeong	$a_0 + a_1 X + a_2 X^2 + a_3 X^3$	0.067	−0.007	−0.058	0.009
Beijing-CAMS	$a_0 + a_1 X + a_2 X^2 + a_3 X^3$	2.211	0.081	0.007	0.006
Beijing	$a_0 + a_1 X + a_2 X^2 + a_3 X^3$	2.360	1.924	0.008	0.003

Table A3. *Cont.*

AERONET Sites	Terra, Aqua MODIS	a_0	a_1	a_2	a_3
Bhola	$a_0 + a_1 X + a_2 X^2 + a_3 X^3$	1.900	4.394	0.003	0.001
Chen−Kung_Univ.	$a_0 + a_1 X + a_2 X^2 + a_3 X^3$	2.056	2.996	0.004	0.002
Chiang_Mai_Met_Sta	$a_0 + a_1 X + a_2 X^2 + a_3 X^3$	−0.249	3.419	0.002	0.003
Dalanzadgad	$a_0 + a_1 X + a_2 X^2 + a_3 X^3$	−0.134	0.644	0.002	0.003
Dhaka−Univ.	$a_0 + a_1 X + a_2 X^2 + a_3 X^3$	0.891	3.390	0.004	0.000
Dongsha_Island	$a_0 + a_1 X + a_2 X^2 + a_3 X^3$	−0.559	1.871	0.145	0.152
Doi_Ang−Khang	$a_0 + a_1 X + a_2 X^2 + a_3 X^3$	−1.041	3.621	0.005	0.003
EPA−NCU	$a_0 + a_1 X + a_2 X^2 + a_3 X^3$	−0.482	2.302	0.002	0.002
Fukuoka	$a_0 + a_1 X + a_2 X^2 + a_3 X^3$	−1.172	2.937	0.003	0.001
Gangneung_WNU	$a_0 + a_1 X + a_2 X^2 + a_3 X^3$	−1.225	2.614	0.004	0.002
Gosan_SNU	$a_0 + a_1 X + a_2 X^2 + a_3 X^3$	−1.166	3.366	0.003	0.001
Hongkong_PolyU	$a_0 + a_1 X + a_2 X^2 + a_3 X^3$	0.453	2.793	0.003	0.000
Irkutsk	$a_0 + a_1 X + a_2 X^2 + a_3 X^3$	−0.354	1.462	0.001	0.002
NGHIA_DO	$a_0 + a_1 X + a_2 X^2 + a_3 X^3$	0.096	−0.389	0.001	0.150
Noto	$a_0 + a_1 X + a_2 X^2 + a_3 X^3$	0.078	−0.332	0.058	0.098
Omkoi	$a_0 + a_1 X + a_2 X^2 + a_3 X^3$	0.295	2.091	0.002	0.000
Seoul_SNU	$a_0 + a_1 X + a_2 X^2 + a_3 X^3$	2.824	2.907	0.004	0.002
Shirahama	$a_0 + a_1 X + a_2 X^2 + a_3 X^3$	0.880	1.930	0.002	0.000
Son_La	$a_0 + a_1 X + a_2 X^2 + a_3 X^3$	−0.142	2.561	0.034	0.028
Taipei_CWB	$a_0 + a_1 X + a_2 X^2 + a_3 X^3$	2.560	2.795	−1.220	0.001
Ussuriysk	$a_0 + a_1 X + a_2 X^2 + a_3 X^3$	−4.129	4.903	0.081	0.012
XiangHe	$a_0 + a_1 X + a_2 X^2 + a_3 X^3$	3.890	4.613	0.006	0.002
Yonsei_Univ.	$a_0 + a_1 X + a_2 X^2 + a_3 X^3$	3.113	2.958	0.004	0.000

Table A4. Summary coefficients of Suomi-NPP/VIIRS AOD products during 2016 in training data ($X = AOD$).

AERONET Sites	Suomi-NPP VIIRS	a_0	a_1	a_2	a_3
Anmyon	$a_0 + a_1 X + a_2 X^2 + a_3 X^3$	3.012	2.703	0.003	0.000
Baengnyeong	$a_0 + a_1 X + a_2 X^2 + a_3 X^3$	0.057	−0.330	0.031	0.021
Beijing-CAMS	$a_0 + a_1 X + a_2 X^2 + a_3 X^3$	−1.873	0.988	2.162	1.010
Beijing	$a_0 + a_1 X + a_2 X^2 + a_3 X^3$	−1.870	0.576	1.801	0.003
Bhola	$a_0 + a_1 X + a_2 X^2 + a_3 X^3$	−1.880	0.271	2.783	0.002
Chen−Kung_Univ.	$a_0 + a_1 X + a_2 X^2 + a_3 X^3$	−3.284	0.571	0.187	1.446
Chiang_Mai_Met_Sta	$a_0 + a_1 X + a_2 X^2 + a_3 X^3$	0.115	3.055	0.004	0.009
Dalanzadgad	$a_0 + a_1 X + a_2 X^2 + a_3 X^3$	0.061	0.449	0.003	0.003
Dhaka−Univ.	$a_0 + a_1 X + a_2 X^2 + a_3 X^3$	−3.810	0.310	0.003	0.000
Dongsha_Island	$a_0 + a_1 X + a_2 X^2 + a_3 X^3$	−1.054	2.363	0.003	0.001
Doi_Ang−Khang	$a_0 + a_1 X + a_2 X^2 + a_3 X^3$	2.306	0.886	0.004	0.001
EPA−NCU	$a_0 + a_1 X + a_2 X^2 + a_3 X^3$	−2.434	4.254	0.005	0.001
Fukuoka	$a_0 + a_1 X + a_2 X^2 + a_3 X^3$	−3.952	5.716	0.003	0.001
Gangneung_WNU	$a_0 + a_1 X + a_2 X^2 + a_3 X^3$	1.447	−1.642	−0.532	0.001
Gosan_SNU	$a_0 + a_1 X + a_2 X^2 + a_3 X^3$	−1.665	3.865	0.004	0.001
Hongkong_PolyU	$a_0 + a_1 X + a_2 X^2 + a_3 X^3$	0.487	1.854	0.000	0.010
Irkutsk	$a_0 + a_1 X + a_2 X^2 + a_3 X^3$	−0.419	1.527	0.004	0.002
NGHIA_DO	$a_0 + a_1 X + a_2 X^2 + a_3 X^3$	0.075	−0.577	0.093	0.112
Noto	$a_0 + a_1 X + a_2 X^2 + a_3 X^3$	0.062	−0.412	0.061	0.085
Omkoi	$a_0 + a_1 X + a_2 X^2 + a_3 X^3$	−0.328	2.214	0.003	0.005
Seoul_SNU	$a_0 + a_1 X + a_2 X^2 + a_3 X^3$	−0.729	3.079	0.004	0.002
Shirahama	$a_0 + a_1 X + a_2 X^2 + a_3 X^3$	−2.624	3.674	0.003	0.001
Son_La	$a_0 + a_1 X + a_2 X^2 + a_3 X^3$	0.405	2.245	0.002	0.010
Taipei_CWB	$a_0 + a_1 X + a_2 X^2 + a_3 X^3$	−2.322	0.622	0.004	0.001
Ussuriysk	$a_0 + a_1 X + a_2 X^2 + a_3 X^3$	−0.097	0.883	0.372	0.001
XiangHe	$a_0 + a_1 X + a_2 X^2 + a_3 X^3$	−2.500	−0.561	0.038	0.684
Yonsei_Univ.	$a_0 + a_1 X + a_2 X^2 + a_3 X^3$	−2.670	0.610	0.250	1.051

Table A5. Seasonal comparison statistics for composite, satellites, and AEORNET AOD products at 500 nm from January to December 2017.

Comparison	Season	N	R	RMSE	MB	MAE
Composite- AERONET	Spring	1372	0.64	0.24	−0.08	0.14
	Summer	800	0.74	0.27	−0.04	0.13
	Fall	1860	0.57	0.26	0.00	0.10
	Winter	2034	0.71	0.22	−0.06	0.14
AHI-AE RONET	Spring	748	0.22	0.37	−0.10	0.17
	Summer	320	0.48	0.34	−0.08	0.11
	Fall	669	0.13	0.23	−0.06	0.09
	Winter	778	0.17	0.36	−0.11	0.16
GOCI-AERONET	Spring	963	0.28	0.38	−0.09	0.17
	Summer	422	0.50	0.35	−0.06	0.12
	Fall	786	0.39	0.24	−0.06	0.09
	Winter	658	0.22	0.35	−0.12	0.15
MODIS-AERONET	Spring	184	0.60	0.17	−0.14	0.16
	Summer	238	0.46	0.15	−0.08	0.11
	Fall	736	0.76	0.26	−0.05	0.09
	Winter	648	0.75	0.25	−0.12	0.15
VIIRS-AERONET	Spring	150	0.73	0.16	−0.14	0.15
	Summer	193	0.83	0.15	−0.08	0.11
	Fall	573	0.75	0.24	−0.06	0.09
	Winter	467	0.70	0.14	−0.13	0.15

Table A6. Spatial comparison statistics for composite, satellites, and AEORNET AOD products at 500 nm from January to December 2017.

Comparison	Region	N	R	RMSE	MB	MAE
Composite-AERONET	Korea	2064	0.65	0.23	−0.08	0.14
	China	1313	0.74	0.30	−0.06	0.23
	Japan	353	0.48	0.18	−0.01	0.06
	Taiwan	2336	0.67	0.21	−0.03	0.12
AHI-AERONET	Korea	680	0.13	0.34	−0.12	0.15
	China	557	0.18	0.35	−0.17	0.22
	Japan	76	0.16	0.17	−0.03	0.05
	Taiwan	1202	0.40	0.32	−0.06	0.12
GOCI-AERONET	Korea	2011	0.40	0.35	−0.06	0.16
	China	389	0.30	0.37	−0.15	0.25
	Japan	401	0.29	0.20	−0.01	0.08
	Taiwan	28	0.52	0.31	−0.10	0.10
MODIS-AERONET	Korea	675	0.60	0.14	−0.12	0.15
	China	356	0.81	0.29	−0.16	0.23
	Japan	130	0.45	0.16	−0.03	0.05
	Taiwan	645	0.64	0.21	−0.08	0.11
VIIRS-AERONET	Korea	575	0.70	0.14	−0.13	0.14
	China	288	0.85	0.37	−0.17	0.22
	Japan	82	0.61	0.16	−0.04	0.05
	Taiwan	438	0.66	0.11	−0.09	0.11

References

1. Kaufman, Y.J.; Didier, T.; Olivier, B. A satellite view of aerosols in the climate system. *Nature* **2002**, *419*, 215–223. [CrossRef] [PubMed]
2. Adler, G.; Haspel, C.; Moise, T.; Rudich, Y. Optical extinction of highly porous aerosol following atmospheric freeze drying. *J. Geophys. Res. Atmos.* **2014**, *119*, 6768–6787. [CrossRef]

3.   Ghan, S.J.; Liu, X.; Easter, R.C.; Zaveri, R.; Rasch, P.J.; Yoon, J.-H.; Eaton, B. Toward a minimal representation of aerosols in climate models: Comparative decomposition of aerosol direct, semidirect, and indirect radiative forcing. *J. Clim.* **2012**, *25*, 6461–6476. [CrossRef]

4.   Zhang, K.; Wan, H.; Liu, X.; Ghan, S.J.; Kopperman, G.J.; Ma, P.-L.; Rasch, P.J. On the use of nudging for aerosol–climate model intercomparison studies. *Atmos. Chem. Phys.* **2014**, *14*, 8631–8645. [CrossRef]

5.   Tiwari, S.; Ramachandran, S. Study of aerosol-cloud interaction over Indo-Gangetic Basin during normal monsoon and drought years. In Proceedings of the American Geophysical Union, Fall Meeting, New Orleans, LA, USA, 11–15 December 2017. Abstract #A51G-2149.

6.   Haywood, J.; Boucher, O. Estimates of the direct and indirect radiative forcing due to tropospheric aerosols: A review. *Rev. Geophys.* **2000**, *38*, 513–543. [CrossRef]

7.   Heald, C.L.; Henze, D.K.; Horowitz, L.W.; Feddema, J.; Lamarque, J.-F.; Guenther, A.; Hess, P.G.; Vitt, F.; Seinfeld, J.H.; Goldstein, A.H.; et al. Predicted change in global secondary organic aerosol concentrations in response to future climate, emissions, and land use change. *J. Geophys. Res.* **2008**, *113*, D05211. [CrossRef]

8.   Anderson, T.L.; Charlson, R.J.; Schwartz, S.E.; Knutti, R.; Boucher, O.; Rodhe, H.; Heintzenberg, J. Climate forcing by Aerosols—A hazy picture. *Science* **2003**, *300*, 1103–1104. [CrossRef] [PubMed]

9.   Ramachandran, S.; Rengarajan, R.; Sarin, M.M. Atmospheric carbonaceous aerosols: Issues, radiative forcing and climate impacts. *Curr. Sci.* **2009**, *97*, 18–20.

10. Engel-Cox, J.A.; Christopher, H.H.; Coutant, B.W.; Hoff, R.M. Qualitative and quantitative evaluation of MODIS satellite sensor data for regional and urban scale air quality. *Atmos. Environ.* **2004**, *38*, 2495–2509. [CrossRef]

11. Dokery, D.W.; CAPope Xiping, X.; Spengler, J.; Ware, J.; Fay, M. An association between air pollution and mortality in 6 US cities. *N. Engl. J. Med.* **1993**, *329*, 1735–1739.

12. Pope, C.A., III; Ezzati, M.; Dockery, D.W. Fine-particulate air pollution and life expectancy in the United States. *N. Engl. J. Med.* **2009**, *360*, 376–386. [CrossRef]

13. Van Donkelaar, A.; Martin, R.V.; Brauer, M.; Kahn, R.; Levy, R.; Verduzco, C.; Villeneuve, P. Global estimates of ambient fine particulate matter concentrations from satellite-based aerosol optical depth: Development and application. *Environ. Health Perspect.* **2010**, *118*, 847–855. [CrossRef] [PubMed]

14. Lim, S.; Lee, M.; Lee, G.; Kim, S.; Yoon, S.; Kang, K. Ionic and carbonaceous compositions of PM 10, PM 2.5 and PM 1.0 at Gosan ABC Superstation and their ratios as source signature. *Atmos. Chem. Phys.* **2012**, *12*, 2007–2024. [CrossRef]

15. Chan, C.; Chan, L. Effect of meteorology and air pollutant transport on ozone episodes at a subtropical coastal Asian city, Hong Kong. *J. Geophys. Res. Atmos.* **2000**, *105*, 20707–20724. [CrossRef]

16. Radojevic, M. Chemistry of forest fires and regional haze with emphasis on Southeast Asia. *Pure Appl. Geophys.* **2003**, *160*, 157–187. [CrossRef]

17. Luan, Y.; Jaeglé, L. Composite study of aerosol export events from East Asia and North America. *Atmos. Chem. Phys.* **2013**, *13*, 1221–1242. [CrossRef]

18. Zhang, W.; Gu, X.; Xu, H.; Yu, T.; Zheng, F. Assessment of OMI near-UV aerosol optical depth over Central and East Asia. *J. Geophys. Res. Atmos.* **2016**, *121*, 382–398. [CrossRef]

19. Kaufman, Y.J.; Koren, I.; Remer, L.A.; Rosenfeld, D.; Rudich, Y. The effect of smoke, dust, and pollution aerosol on shallow cloud development over the Atlantic Ocean. *Proc. Natl. Acad. Sci. USA* **2005**, *102*, 11207–11212. [CrossRef]

20. Kahn, R.A.; Gaitley, B.J.; Garay, M.J.; Diner, D.J.; Eck, T.F.; Smirnov, A.; Holben, B.N. Multiangle Imaging SpectroRadiometer global aerosol product assessment by comparison with the Aerosol Robotic Network. *J. Geophys. Res. Atmos.* **2010**, *115*. [CrossRef]

21. Kinne, S. Remote sensing data combinations: Superior global maps for aerosol optical depth. In *Satellite Aerosol Remote Sensing over Land*; Kokhanovsky, A.A., de Leeuw, G., Eds.; Springer: Berlin, Germany, 2009.

22. Shao, P.; Xin, J.; An, J.; Kong, L.; Wang, B.; Wang, J.; Wang, Y.; Wu, D. The empirical relationship between PM2.5 and AOD in Nanjing of the Yangtze River Delta. *Atmos. Pollut. Res.* **2017**, *8*, 233–243. [CrossRef]

23. Zheng, Y.; Che, H.; Yang, L.; Chen, J.; Wang, Y.; Xia, X.; Zhao, H.; Wang, H.; Wang, D.; Gui, K. Optical and radiative properties of aerosols during a severe haze episode over the North China Plain in December. *J. Meteorol. Res.* **2016**, *31*, 1045–1061. [CrossRef]

24. Dubovik, O.; Smirnov, A.; Holben, B.N.; King, M.D.; Kaufman, Y.J.; Eck, T.F.; Slutsker, I. Accuracy assessments of aerosol optical properties retrieved from Aerosol Robotic Network AERONET) Sun and sky radiance measurements. *J. Geophys. Res. Atmos.* **2000**, *105*, 9791–9806. [CrossRef]

25. Creamean, J.; Suski, K.; Rosenfeld, D.; Cazorla, A.; DeMott, P.; Sullivan, R.; White, A.; Ralph, F.; Minnis, P.; Comstock, J.; et al. Dust and biological aerosols from the Sahara and Asia influence precipitation in the western US. *Science* **2013**, *339*, 1572–1578. [CrossRef] [PubMed]

26. Van Donkelaar, A.; Martin, R.V.; Park, R.J. Estimating ground-level PM2.5 using aerosol optical depth determined from satellite remote sensing. *J. Geophys. Res. Atmos.* **2006**, *111*, D21. [CrossRef]

27. Wang, J.; Christopher, S.A. Intercomparison between satellite derived aerosol optical thickness and PM2.5 mass: Implications for air quality studies. *Geophys. Res. Lett.* **2003**, *30*, 2095. [CrossRef]

28. Zhang, J.; Reid, J. A decadal regional and global trend analysis of the aerosol optical depth using a data-assimilation grade over-water MODIS and Level 2 MISR aerosol products. *Atmos. Chem. Phys.* **2010**, *10*, 10949–10963. [CrossRef]

29. Levy, R.C.; Munchak, L.A.; Mattoo, S.; Patadia, F.; Remer, L.A.; Holz, R.E. Towards a long-term global aerosol optical depth record: Applying a consistent aerosol retrieval algorithm to MODIS and VIIRS-observed reflectance. *Atmos. Meas. Tech.* **2015**, *8*, 4083–4110. [CrossRef]

30. Sorek-Hamer, M.; Kloog, I.; Koutrakis, P.; Strawa, A.W.; Chatfield, R.; Cohen, A.; Ridgway, W.L.; Broday, D.M. Assessment of PM2.5 concentrations over bright surfaces using MODIS satellite observations. *Remote Sens. Environ.* **2015**, *163*, 180–185. [CrossRef]

31. Wei, J.; Li, Z.; Suj, L.; Peng, Y.; Liu, L.; He, L.; Qin, W.; Cribb, M. MODIS Collection 6.1 3 km resolution aerosol optical depth product: Global evaluation and uncertainty analysis. *Atmos. Environ.* **2020**, *240*, 117768. [CrossRef]

32. Li, C.; Li, J. Impact of aerosol vertical distribution on aerosol optical depth retrieval from passive satellite sensors. *Remote Sens.* **2020**, *12*, 1524. [CrossRef]

33. Xue, Y.; Xu, H.; Mei, L.; Guang, J.; Guo, J.; Li, Y.; Hou, T.; Li, C.; Yang, L.; He, X. Merging aerosol optical depth data from multiple satellite missions to view agricultural biomass burning in Central and East China. *Atmos. Chem. Phys. Discuss.* **2012**, *12*, 10461–10492.

34. Zhang, X.; Tang, Q. Combining satellite precipitation and long-term ground observations for hydrological monitoring in China. *J. Geophys. Res. Atmos.* **2015**, *120*, 6426–6443. [CrossRef]

35. Kokhanovsky, A.A.; Breon, F.M.; Cacciari, A.; Carboni, E.; Diner, D.; Di Nicolantonio, W.; Grainger, R.G.; Grey, W.M.F.; Holler, R.; Lee, K.-H.; et al. Aerosol remote sensing over land: A comparison of satellite retrievals using different algorithms and instruments. *Atmos. Res.* **2007**, *85*, 372–394. [CrossRef]

36. De Leeuw, G.; Holzer-Popp, T.; Bevan, S.; Davies, W.; Descloitres, J.; Grainger, R.G.; Griesfeller, J.; Heckel, A.; Kinne, S.; Klüser, L. Evaluation of seven European aerosol optical depth retrieval algorithms for climate analysis. *Remote Sens. Environ.* **2015**, *162*, 295–315. [CrossRef]

37. Nirala, M. Multi-sensor data fusion of aerosol optical thickness. *Int. J. Remote Sens.* **2008**, *29*, 2127–2136. [CrossRef]

38. Heo, J.-H.; Ryu, G.-H.; Sohn, E.-H.; Jang, J.-D. Application of Cumulative Distribution Functions to Compositing Precipitable Water with Low Earth Orbit Satellite Data. *Asia-Pac. J. Atmos. Sci.* **2020**, *56*, 57–75. [CrossRef]

39. Wei, X.; Chang, N.B.; Bai, K.; Gao, W. Satellite remote sensing of aerosol optical depth: Advances, challenges, and perspectives. *Crit. Rev. Environ. Sci. Technol.* **2020**, *50*, 1640–1725. [CrossRef]

40. Li, J.; Li, X.; Carlson, B.E.; Kahn, R.A.; Lacis, A.A.; Dubovik, O.; Nakajima, T. Reducing multisensor satellite monthly mean aerosol optical depth uncertainty: 1. Objective assessment of current AERONET locations. *J. Geophys. Res. Atmos.* **2016**, *121*, 13,609–13,627. [CrossRef] [PubMed]

41. Kidder, S.Q.; Jones, A.S. A blended satellite total precipitable water product for operational forecasting. *J. Atmos. Ocean. Technol.* **2007**, *24*, 74–81. [CrossRef]

42. Heo, J.H.; Ryu, G.-H.; Jang, J.-D. Optimal interpolation of precipitable water using low earth orbit and numerical weather prediction data. *Remote Sens.* **2018**, *10*, 436.

43. Bain, L.J. *Statistical Analysis of Reliability and Life Testing Model*; Marceland Dekker Inc.: New York, NY, USA, 1976.

44. Yumimoto, K.; Nagao, T.M.; Kikuchi, M.; Sekiyama, T.T.; Murakami, H.; Tanaka, T.Y.; Ogi, A.; Irie, H.; Khatri, P.; Okumura, H. Aerosol data assimilation using data from Himawari-8, a next-generation geostationary meteorological satellite. *Geophys. Res. Lett.* **2016**, *43*, 5886–5894. [CrossRef]

45. Bessho, K.; Date, K.; Hayashi, M.; Ikeda, A.; Imai, T.; Inoue, H.; Kumagai, Y.; Miyakawa, T.; Murata, H.; Ohno, T.; et al. An introduction to Himawari-8/9—Japan's new-generation geostationary meteorological satellites. *J. Meteorol. Soc. Jpn. Ser. II* **2016**, *94*, 151–183. [CrossRef]

46. Yan, X.; Li, Z.; Luo, N.; Shi, W.; Zhao, W.; Yang, X.; Jin, J. A minimum albedo aerosol retrieval method for the new-generation geostationary meteorological satellite Himawari-8. *Atmos. Res.* **2018**, *207*, 14–27. [CrossRef]

47. Yumimoto, K.; Tanaka, T.Y.; Yoshida, M.; Kikuchi, M.; Nagao, T.M.; Murakami, H.; Maki, T. Assimilation and forecasting experiment for heavy Siberian wildfire smoke in May 2016 with Himawari-8 aerosol optical thickness. *J. Meteorol. Soc. Jpn. Ser. II* **2018**. [CrossRef]

48. Fukuda, S.; Nakajima, T.; Takenaka, H.; Higurashi, A.; Kikuchi, N.; Nakajima, T.Y.; Ishida, H. New approaches to removing cloud shadows and evaluating the 380 nm surface reflectance for improved aerosol optical thickness retrievals from the GOSAT/TANSO-Cloud and Aerosol Imager. *J. Geophys. Res. Atmos.* **2013**, *118*, 13,520–13,531. [CrossRef]

49. Yoshida, M.; Kikuchi, M.; Nagao, T.M.; Murakami, H.; Nomaki, T.; Higurash, A. Common retrieval of aerosol properties for imaging satellite sensors. *J. Meteorol. Soc. Jpn. Ser. II* **2018**. [CrossRef]

50. Wang, W.; Mao, F.; Pan, Z.; Gong, W.; Yoshida, M.; Zou, B.; Ma, H. Evaluating aerosol optical depth from Himawari-8 with Sun photometer network. *J. Geophys. Res. Atmos.* **2019**, *124*, 5516–5538. [CrossRef]

51. Choi, J.K.; Park, Y.J.; Ahn, J.H.; Lim, H.S.; Eom, J.; Ryu, J.H. GOCI, the world's first geostationary ocean color observation satellite, for the monitoring of temporal variability in coastal water turbidity. *J. Geophys. Res. Ocean.* **2012**, *117*. [CrossRef]

52. Choi, M.; Kim, J.; Lee, J.; Kim, M.; Je Park, Y.; Jeong, U.; Kim, W.; Holben, B.; Eck, T.F.; Lim, J.H.; et al. GOCI Yonsei Aerosol Retrieval (YAER) algorithm and validation during DRAGON-NE Asia 2012 campaign. *Atmos. Meas. Tech. Discuss.* **2015**, *8*, 9565–9609.

53. Choi, M.; Kim, J.; Lee, J.; Kim, M.; Park, Y.-J.; Holben, B.; Eck, T.F.; Li, Z.; Song, C.H. GOCI Yonsei aerosol retrieval version 2 products: An improved algorithm and error analysis with uncertainty estimation from 5-year validation over East Asia. *Atmos. Meas. Tech.* **2018**, *11*, 385–408. [CrossRef]

54. Kaufman, Y.J.; Tanre, D. Strategy for direct and indirect methods for correcting the aerosol effect on remote sensing: From AVHRR to EOS-MODIS. *Remote Sens. Environ.* **1996**, *55*, 65–79. [CrossRef]

55. Levy, R.C.; Remer, L.A.; Kleidman, R.G.; Mattoo, S.; Ichoku, C.; Kahn, R.; Eck, T.F. Global evaluation of the Collection 5 MODIS dark-target aerosol products over land. *Atmos. Chem. Phys.* **2010**, *10*, 10399–10420. [CrossRef]

56. Bilal, M.; Nichol, J.E. Evaluation of MODIS aerosol retrieval algorithms over the Beijing-Tianjin-Hebei region during low to very high pollution events. *J. Geophys. Res. Atmos.* **2015**, *120*, 7941–7957. [CrossRef]

57. Levy, R.C.; Mattoo, S.; Munchak, L.A.; Remer, L.A.; Sayer, A.M.; Patadia, F.; Hsu, N.C. The Collection 6 MODIS aerosol products over land and ocean. *Atmos. Meas. Tech.* **2013**, *6*, 2989. [CrossRef]

58. Nichol, J.; Bilal, M. Validation of MODIS 3 km resolution aerosol optical depth retrievals over Asia. *Remote Sens.* **2016**, *8*, 328. [CrossRef]

59. Remer, L.A.; Kaufman, Y.J.; Tanré, D.; Mattoo, S.; Chu, D.A.; Martins, J.V.; Li, R.R.; Ichoku, C.; Levy, R.C.; Kleidman, R.G.; et al. The MODIS aerosol algorithm, products, and validation. *J. Atmos. Sci.* **2005**, *62*, 947–973. [CrossRef]

60. Chu, D.; Ichoku, C.; Remer, L.A.; Tanre, D.; Holben, B.N. Validation of MODIS aerosol optical depth retrieval over land. *Geophys. Res. Lett.* **2002**, *29*, MOD2-1–MOD2-4. [CrossRef]

61. Sayer, A.M.; Hsu, N.C.; Bettenhausen, C.; Jeong, M.-J. Validation and uncertainty estimates for MODIS Collection 6 Deep Blue aerosol data. *J. Geophys. Res. Atmos.* **2013**, *118*, 7864–7872. [CrossRef]

62. Remer, L.A.; Mattoo, S.; Levy, R.C.; Munchak, L.A. MODIS 3 km aerosol product: Algorithm and global perspective. *Atmos. Meas. Tech.* **2013**, *6*, 1829–1844. [CrossRef]

63. Huang, J.; Kondragunta, S.; Laszlo, I.; Liu, H.; Remer, L.A.; Zhang, H.; Superczynski, S.; Ciren, P.; Holben, B.N.; Petrenko, M. Validation and expected error estimation of Suomi-NPP VIIRS aerosol optical thickness and Ångström exponent with AERONET. *J. Geophys. Res. Atmos.* **2016**, *121*, 7139–7160. [CrossRef]

64. Jackson, J.M.; Liu, H.; Laszlo, I.; Kondragunta, S.; Remer, L.A.; Huang, J.; Huang, H.C. Suomi-NPP VIIRS aerosol algorithms and data products. *J. Geophys. Res. Atmos.* **2013**, *118*, 12673–12689. [CrossRef]

65. Kotchenova, S.Y.; Vermote, E.F. Validation of a vector version of the 6S radiative transfer code for atmospheric correction of satellite data. Part II. Homogeneous Lambertian and anisotropic surfaces. *Appl. Opt.* **2007**, *46*, 4455–4464. [CrossRef]

66. Vermote, E.F.; Kotchenova, S. Atmospheric correction for the monitoring of land surfaces. *J. Geophys. Res. Atmos.* **2008**, *113*. [CrossRef]

67. Holben, B.N.; Eck, T.F.; Slutsker, I.; Tanre, D.; Buis, J.P.; Setzer, A.; Vermote, E.; Reagan, J.A.; Kaufman, Y.J.; Nakajima, T.; et al. AERONET—A federated instrument network and data archive for aerosol characterization. *Remote Sens. Environ.* **1998**, *66*, 1–16. [CrossRef]

68. Holben, B.N.; Tanre, D.; Smirnov, A.; Eck, T.F.; Slutsker, I.; Abuhassan, N.; Newcomb, W.W.; Schafer, J.; Chatenet, B.; Lavenue, F.; et al. An emerging ground-based aerosol climatology: Aerosol optical depth from AERONET. *J. Geophys. Res. Atmos.* **2001**, *106*, 12067–12097. [CrossRef]

69. Shin, S.-K.; Tesche, M.; Müller, D.; Noh, Y. Absorption aerosol optical depth components from AERONET observations of mixed dust plumes. *Atmos. Meas. Tech.* **2019**, *12*, 607–618. [CrossRef]

70. Dey, S.; Tripathi, S.N.; Singh, R.P.; Holben, B.N. Retrieval of black carbon and specific absorption over Kanpur city, northern India during 2001–2003 using AERONET data. *Atmos. Environ.* **2006**, *40*, 445–456. [CrossRef]

71. Alam, K.; Trautmann, T.; Blaschke, T. Aerosol optical properties and radiative forcing over mega-city Karachi. *Atmos. Res.* **2011**, *101*, 773–782. [CrossRef]

72. Alam, K.; Trautmann, T.; Blaschke, T.; Subhan, F. Changes in aerosol optical properties due to dust storms in the Middle East and Southwest Asia. *Remote Sens. Environ.* **2014**, *143*, 216–227. [CrossRef]

73. Bibi, H.; Alam, K.; Chishtie, F. Intercomparison of MODIS, MISR, OMI, and CALIPSO aerosol optical depth retrievals for four locations on the Indo-Gangetic plains and validation against AERONET data. *Atmos. Environ.* **2015**, *111*, 113–126. [CrossRef]

74. Holben, B.N.; Tanré, A.D.; Smirnov, T.F.; Eck, I.; Slutsker, O.; Dubovik, F.; Lavenu, N.; Abuhassen, C.B. Optical properties of aerosols from long term ground-based aeronet measurements. In Proceedings of the ALPS99, Meribel, France, 17–23 January 1999.

75. Schmid, B.; Michalsky, J.; Ttalthore, R.; Beauharnois, M.; Harrison, L.; Livingston, J.; Russell, P.; Holben, B.; Eck, T.; Stairnov, A. Comparison of aerosol optical depth from four solar radiometers during the fall 1997 ARM intensive observation period. *Geophys. Res. Lett.* **1999**, *26*, 2725–2728. [CrossRef]

76. Gupta, P.; Remer, L.A.; Levy, R.C.; Mattoo, S. Validation of MODIS 3 km land aerosol optical depth from NASA's EOS Terra and Aqua missions. *Atmos. Meas. Tech.* **2018**, *11*, 3145–3159. [CrossRef]

77. Deng, P.; Zhang, M.; Guo, H.; Xu, C.; Bing, J.; Jia, J. Error analysis and correction of the daily GSMaP products over Hanjiang River Basin of China. *Atmos. Res.* **2018**, *214*, 121–134. [CrossRef]

78. Sheffield, J.; Wood, E.F.; Chaney, N.; Guan, K.; Sadri, S.; Yuan, X.; Demuth, S. A drought monitoring and forecasting system for sub-Sahara African water resources and food security. *Bull. Am. Meteorol. Soc.* **2014**, *95*, 861–882. [CrossRef]

79. Liu, M.; Shen, Y.; Qi, Y.; Wang, Y.; Geng, X. Changes in precipitation and drought extremes over the past half century in China. *Atmosphere* **2019**, *10*, 203. [CrossRef]

80. Reichle, R.H.; Koster, R.D. Bias reduction in short records of satellite soil moisture. *Geophys. Res. Lett.* **2004**, *31*, L19501. [CrossRef]

81. Liu, Y.; van Dijk, A.I.J.M.; de Jeu, R.A.M.; Holmes, T.R.H. An analysis of spatiotemporal variations of soil and vegetation moisture from a 29-year satellite-derived data set over mainland Australia. *Water Resour. Res.* **2009**, *45*. [CrossRef]

82. Klippel, S.; Wieczorek, M.; Schumann, M.; Krause, E.; Marg, B.; Seidel, T.; Meyer, T.; Knapp, E.W.; Freund, C. Multivalent binding of formin-binding protein 21 FBP21)-tandem-WW domains fosters protein recognition in the pre-spliceosome. *J. Biol. Chem.* **2011**, *286*, 38478–38487. [CrossRef] [PubMed]

83. Nalder, I.A.; Wein, R.W. Spatial interpolation of climatic normals: Test of a new method in the Canadian boreal forest. *Agric. For. Meteorol.* **1998**, *92*, 211–225. [CrossRef]

84. Chao, L.; Zhang, K.; Li, Z.; Zhu, Y.; Wang, J.; Yu, Z. Geographically weighted regression based methods for merging satellite and gauge precipitation. *J. Hydrol.* **2018**, *558*, 275–289. [CrossRef]

85. Dinku, T.; Hailemariam, K.; Maidment, R.; Tarnavsky, E.; Connor, S. Combined use of satellite estimates and rain gauge observations to generate high-quality historical rainfall time series over Ethiopia. *Int. J. Climatol.* **2014**, *34*, 2489–2504. [CrossRef]

86. Manz, B.; Buytaert, W.; Zulkafli, Z.; Lavado, W.; Willems, B.; Alberto Robles, L.; Rodriguez-Sanchez, J.-P. High-resolution satellite-gauge merged precipitation climatologies of the Tropical Andes. *J. Geophys. Res. Atmos.* **2016**, *121*, 1190–1207. [CrossRef]

87. Lloyd, C. Assessing the effect of integrating elevation data into the estimation of monthly precipitation in Great Britain. *J. Hydrol.* **2005**, *308*, 128–150. [CrossRef]

88. Draxler, R.R.; Hess, G. An overview of the HYSPLIT_4 modelling system for trajectories. *Aust. Meteorol. Mag.* **1998**, *47*, 295–308.

89. Draxler, R.R. The use of global and mesoscale meteorological model data to predict the transport and dispersion of tracer plumes over Washington, DC. *Weather Forecast.* **2006**, *21*, 383–394. [CrossRef]

90. Fleming, Z.L.; Monks, P.S.; Manning, A.J. Untangling the influence of air-mass history in interpreting observed atmospheric composition. *Atmos. Res.* **2012**, *104*, 1–39. [CrossRef]

91. Efstathiou, C.; Isukapalli, S.; Georgopoulos, P. A mechanistic modeling system for estimating large-scale emissions and transport of pollen and co-allergens. *Atmos. Environ.* **2011**, *45*, 2260–2276. [CrossRef]

92. Stunder, B.J.B.; Heffter, J.L.; Draxler, R.R. Airborne volcanic ash forecast area reliability. *Weather Forecast.* **2007**, *22*, 1132–1139. [CrossRef]

93. Pasken, R.; Pietrowicz, J.A. Using dispersion and mesoscale meteorological models to forecast pollen concentrations. *Atmos. Environ.* **2005**, *39*, 7689–7701. [CrossRef]

94. Chen, B.; Stein, A.F.; Maldonado, P.G.; de la Campa, A.M.S.; Gonzalez-Castanedo, Y.; Castell, N.; Jesus, D. Size distribution and concentrations of heavy metals in atmospheric aerosols originating from industrial emissions as predicted by the HYSPLIT model. *Atmos. Environ.* **2013**, *71*, 234–244. [CrossRef]

95. Gaiero, D.M.; Simonella, L.; Gasso, S.; Gili, S.; Stein, A.F.; Soas, P. Ground/satellite observations and atmospheric modeling of dust storms originating in the high Puna-Altiplano deserts South America): Implications for the interpretation of paleo-climatic archives. *J. Geophys. Res. Atmos.* **2013**, *118*, 3817–3831. [CrossRef]

96. Stein, A.F.; Isakov, V.; Godowitch, J.; Draxler, R.R. A hybrid modeling approach to resolve pollutant concentrations in an urban area. *Atmos. Environ.* **2007**, *41*, 9410–9426. [CrossRef]

97. Bowyer, T.W.; Kephart, R.; Eslinger, P.W.; Friese, J.I.; Miley, H.S.; Saey, P.R.J. Maximum reasonable radioxenon releases from medical isotope production facilities and their effect on monitoring nuclear explosions. *J. Environ. Radioact.* **2013**, *115*, 192–200. [CrossRef]

98. Jeong, H.; Park, M.; Jeong, H.; Hwang, W.; Kim, E.; Han, M. Radiological risk assessment caused by RDD terrorism in an urban area. *Appl. Radiat. Isot.* **2013**, *79*, 1–4. [CrossRef] [PubMed]

99. Jiang, T.; Chen, B.; Chan, K.K.Y.; Xu, B. Himawari-8/AHI and MODIS aerosol optical depths in China: Evaluation and comparison. *Remote Sens.* **2019**, *11*, 1011. [CrossRef]

100. Xiao, Q.; Zhang, H.; Choi, M.; Li, S.; Kondragunta, S.; Kim, J.; Holben, B.; Levy, R.C.; Liu, Y. Evaluation of VIIRS, GOCI, and MODIS Collection 6 AOD retrievals against ground sunphotometer observations over East Asia. *Atmos. Chem. Phys.* **2016**, *16*, 1255. [CrossRef]

101. Bilal, M.; Nazeer, M.; Nichol, J.; Qiu, Z.; Wang, L.; Bleiweiss, M.P.; Lolli, S. Evaluation of Terra-MODIS C6 and C6. 1 aerosol products against Beijing, XiangHe, and Xinglong AERONET sites in China during 2004–2014. *Remote Sens.* **2019**, *11*, 486. [CrossRef]

102. Qi, Y.; Ge, J.; Huang, J. Spatial and temporal distribution of MODIS and MISR aerosol optical depth over northern China and comparison with AERONET. *Chin. Sci. Bull.* **2013**, *58*, 2497–2506. [CrossRef]

103. Wang, L.; Wang, J.X.; Li, Z.; Liu, G.; Li, J. Evaluation of the MODIS aerosol optical depth retrieval over different ecosystems in China during EAST-AIRE. *Atmos. Environ.* **2007**, *41*, 7138–7149. [CrossRef]

104. Li, X.H.; Wang, S.X.; Duan, L.; Hao, J.M.; Nie, Y.F. Carbonaceous aerosol emissions from household biofuel combustion in China. *Environ. Sci. Technol.* **2009**, *43*, 6076–6081. [CrossRef] [PubMed]

105. Anderson, J.C.; Wang, J.; Zeng, J.; Leptoukh, G.; Petrenko, M.; Ichoku, C.; Hu, C. Long-term statistical assessment of Aqua-MODIS aerosol optical depth over coastal regions: Bias characteristics and uncertainty sources. *Tellus B Chem. Phys. Meteorol.* **2013**, *65*, 20805. [CrossRef]

106. Mhawish, A.; Banerjee, T.; Broday, D.M.; Misra, A. Evaluation of MODIS Collection 6 aerosol retrieval algorithms over Indo-Gangetic Plain: Implications of aerosols types and mass loading. *Remote Sens. Environ.* **2017**, *201*, 297–313. [CrossRef]

107. He, L.J.; Wang, L.C.; Lin, A.W.; Zhang, M.; Bilal, M.; Wei, J. Performance of the NPP-VIIRS and Aqua-MODIS aerosol optical depth products over the Yangtze River Basin. *Remote Sens.* **2018**, *10*, 117. [CrossRef]

108. Zhang, Z.; Wu, W.; Fan, M.; Wei, J.; Jin, J.; Tan, Y.; Wang, Q. Validation of Himawari-8 aerosol optical depth retrievals over China. *Atmos. Environ.* **2019**, *199*, 32–44. [CrossRef]

109. Tao, J.; Zhang, L.; Cao, J.; Zhang, R. A review of current knowledge concerning PM 2.5 chemical composition, aerosol optical properties and their relationships across China. *Atmos. Chem. Phys.* **2017**, *17*, 9485. [CrossRef]

110. Husar, R.; Tratt, D.M.; Schichtel, B.A. Asian dust events of April 1998. *J. Geophys. Res. Atmos.* **2001**, *106*, 18317–18330. [CrossRef]

111. Wang, F.; Chen, D.S.; Cheng, S.Y.; Li, J.B.; Li, M.J.; Ren, Z.H. Identification of regional atmospheric PM10 transport pathways using HYSPLIT, MM5-CMAQ and synoptic pressure pattern analysis. *Environ. Model. Softw.* **2010**, *25*, 927–934. [CrossRef]

112. He, L.; Wang, L.; Lin, A.; Zhang, M.; Bilal, M.; Tao, M. Aerosol optical properties and associated direct radiative forcing over the Yangtze River basin during 2001–2015. *Remote Sens.* **2017**, *9*, 746. [CrossRef]

113. Cheng, Z.; Wang, S.X.; Jiang, J.K.; Fu, Q.Y.; Chen, C.H.; Xu, B.Y. Long-term trend of haze pollution and impact of particulate matter in the Yangtze River Delta, China. *Environ. Pollut.* **2013**, *182*, 101–110. [CrossRef]

114. Li, B.; Zhang, J.; Zhao, Y.; Yuan, S.; Zhao, Q.; Shen, G.; Wu, H. Seasonal variation of urban carbonaceous aerosols in a typical city Nanjing in Yangtze River Delta, China. *Atmos. Environ.* **2015**, *106*, 223–231. [CrossRef]

115. Knapp, K.R.; Vonder Haar, T.H.; Kaufman, Y.J. Aerosol optical depth retrieval from GOES-8: Uncertainty study and retrieval validation over South America. *J. Geophys. Res. Atmos.* **2002**, *107*, AAC 2-1–AAC 2-12. [CrossRef]

116. Zhang, W.; Xu, H.; Zhang, L. Assessment of Himawari-8 AHI Aerosol Optical Depth Over Land. *Remote Sens.* **2019**, *11*, 1108. [CrossRef]

117. Naeger, A.R.; Gupta, P.; Zavodsky, B.T.; McGrath, K.M. Monitoring and tracking the trans-Pacific transport of aerosols using multi-satellite aerosol optical depth composites. *Atmos. Meas. Tech.* **2016**, *9*, 2463–2482. [CrossRef]